Vibrational Spectral Emission of Fractional-Principal-Quantum-Energy-Level Molecular Hydrogen

R. L. Mills*, P. Ray, J. Dong, M. Nansteel, B. Dhandapani, J. He
BlackLight Power, Inc.
493 Old Trenton Road
Cranbury, NJ 08512

ABSTRACT

Extreme ultraviolet (EUV) spectroscopy was recorded on microwave discharges of helium with 2% hydrogen. Novel emission lines were observed with energies of $q \cdot 13.6\ eV$ where $q = 1,2,3,4,6,7,8,9,11$ or these lines inelastically scattered by helium wherein $21.2\ eV$ was absorbed in the excitation of $He\ (1s^2)$ to $He\ (1s^1 2p^1)$. These lines matched $H(1/p)$, fractional Rydberg states of atomic hydrogen, formed by a resonant nonradiative energy transfer to He^+. Corresponding emission due to the reaction $2H(1/2) \rightarrow H_2(1/2)$ with vibronic coupling at $E_{D+vib} = p^2 E_{D H_2} \pm \left(\frac{\upsilon^*}{3}\right) E_{vib\ H_2(\upsilon=0\rightarrow\upsilon=1)}$, $\upsilon^* = 1,2,3...$ was observed at the longer wavelengths for $\upsilon^* = 2$ to $\upsilon^* = 32$ and at the shorter wavelengths for $\upsilon^* = 1$ to $\upsilon^* = 16$ where $E_{D H_2}$ and $E_{vib\ H_2(\upsilon=0\rightarrow\upsilon=1)}$ are the experimental bond and vibrational energies of H_2, respectively. Similar emission due to Ne^+ with hydrogen was also observed, and the exothermic reaction was confirmed by the observation of $306 \pm 5\ W$ of excess power generated in $45\ cm^3$ by a compound-hollow-cathode-glow discharge of a neon-hydrogen (99.5/0.5%) mixture corresponding to a power density of $6.8\ MW/m^3$ and an energy balance of at least $-1\ X\ 10^6\ kJ/mole\ H_2$ compared to the enthalpy of combustion of hydrogen of $-241.8\ kJ/mole\ H_2$.

Keywords: EUV spectroscopy, catalysis, vibronic coupling

* To whom correspondence should be addressed. Phone: 609-490-1090; Fax: 609-490-1066; E-mail: rmills@blacklightpower.com

I. Introduction

J. R. Rydberg showed that all of the spectral lines of atomic hydrogen were given by a completely empirical relationship:

$$\bar{\nu} = R\left(\frac{1}{n_f^2} - \frac{1}{n_i^2}\right) \tag{1}$$

where $R = 109{,}677\ cm^{-1}$, $n_f = 1,2,3,...$, $n_i = 2,3,4,...$ and $n_i > n_f$. Bohr, Schrödinger, and Heisenberg each developed a theory for atomic hydrogen that gave the energy levels in agreement with Rydberg's equation.

$$E_n = -\frac{e^2}{n^2 8\pi\varepsilon_o a_H} = -\frac{13.598\ eV}{n^2} \tag{2a}$$

$$n = 1,2,3,... \tag{2b}$$

The excited energy states of atomic hydrogen are given by Eq. (2a) for $n > 1$ in Eq. (2b). The $n = 1$ state is the "ground" state for "pure" photon transitions (i.e. the $n = 1$ state can absorb a photon and go to an excited electronic state, but it cannot release a photon and go to a lower-energy electronic state). However, an electron transition from the ground state to a lower-energy state may be possible by a resonant nonradiative energy transfer such as multipole coupling or a resonant collision mechanism. Processes such as hydrogen molecular bond formation that occur without photons and that require collisions are common [1]. Also, some commercial phosphors are based on resonant nonradiative energy transfer involving multipole coupling [2].

We propose that atomic hydrogen may undergo a catalytic reaction with certain atoms, excimers, and ions which provide a reaction with a net enthalpy of an integer multiple of the potential energy of atomic hydrogen, $m \cdot 27.2\ eV$ wherein m is an integer. The ionization of He^+ to He^{2+}, $Ne^+ + H^+$ to $Ne^{2+} + H$, and $Ne_2{}^*$ to $2Ne^+$ provide a reaction with a net enthalpy equal to two, one, and one times the potential energy of atomic hydrogen, respectively. The theory and supporting data was given previously [3-49]. The reaction involves a nonradiative energy transfer to form a hydrogen atom that is lower in energy than unreacted atomic hydrogen that corresponds to a fractional principal quantum number. That is

$$n = \frac{1}{2}, \frac{1}{3}, \frac{1}{4}, ..., \frac{1}{p}; \quad p \text{ is an integer} \tag{2c}$$

replaces the well known parameter $n = \text{integer}$ in the Rydberg equation for hydrogen excited states. The $n = 1$ state of hydrogen and the $n = \frac{1}{\text{integer}}$ states of hydrogen are nonradiative, but a transition between two nonradiative states, say $n = 1$ to $n = 1/2$, is possible via a nonradiative energy transfer. Thus, a catalyst provides a net positive enthalpy of reaction of $m \cdot 27.2\ eV$ (i.e. it resonantly accepts the nonradiative energy transfer from hydrogen atoms and releases the energy to the surroundings to affect electronic transitions to fractional quantum energy levels). As a consequence of the nonradiative energy transfer, the hydrogen atom becomes unstable and emits further energy until it achieves a lower-energy nonradiative state having a principal energy level given by Eqs. (2a) and (2c).

Prior related studies that support the possibility of a novel reaction of atomic hydrogen which produces hydrogen in fractional quantum states that are at lower energies than the traditional "ground" ($n = 1$) state include extreme ultraviolet (EUV) spectroscopy [3, 4, 13-19, 21-23, 26, 30, 34-36, 38-39], characteristic emission from catalysis and the hydride ion products [8, 11-12, 18, 23, 26], lower-energy hydrogen emission [14-17, 21, 22], plasma formation [3, 4, 8, 11, 18, 23, 26, 30, 34-35, 37-39], Balmer α line broadening [4, 7-8, 11, 13-17, 20, 30, 34], elevated electron temperature [4, 7, 13-16], anomalous plasma afterglow duration [3, 37-38], power generation [7, 11, 15-17, 19, 20, 25, 27, 47-49], and analysis of chemical compounds [5-6, 12, 25, 31, 41-45].

The product of the catalysis reaction of He^+, $H(1/3)$, may further serve as a catalyst to form $H(1/4)$ and $H(1/2)$ [22]. It was reported previously [21] that $H(1/p)$ may react with a proton to form an excited state molecular ion $H_2^*(1/p)^+$ that has a bond energy and vibrational levels that are p^2 times those of the molecular ion comprising uncatalyzed atomic hydrogen where p is an integer. Thus, the excited state spectrum of $H_2^*[n = 1/4; n^* = 2]^+$ was predicted to comprise rotationally broadened vibrational transitions at 1.185 eV increments to the dissociation limit of $H_2[n = 1/4]^+$, $E_D = 42.88\ eV\ (28.92\ nm)$. Extreme ultraviolet (EUV) spectroscopy was recorded on microwave discharges of argon or helium with 10%

hydrogen in the range $10\text{-}65\,nm$. Novel emission lines assigned to vibrational transitions of $H_2^*[n=1/4;n^*=2]^+$ were observed in this range with energies of $\upsilon\cdot 1.185\,eV$, $\upsilon = 17\,to\,38$ that terminated at about $28.9\,nm$ [21].

Two hydrogen atoms react to form a diatomic molecule, the hydrogen molecule, H_2.

$$2H\left[a_H\right] \rightarrow H_2\left[2c' = \sqrt{2}a_o\right] \tag{3}$$

where $2c'$ is the internuclear distance given by

$$2c' = \sqrt{2}a_o \tag{4}$$

where a_o is the Bohr radius. We also propose that the diatomic molecule $H_2(1/p)$ may form by reaction of the corresponding fractional Rydberg state atoms $H(1/p)$

$$2H\left[\frac{a_H}{p}\right] \rightarrow H_2\left[2c' = \frac{\sqrt{2}a_o}{p}\right] \tag{5}$$

where each energy level corresponds to a fractional quantum number that is the reciprocal of an integer p. The derivation of the parameters of $H_2(1/p)$ was published previously [21, 40]. The central field of fractional Rydberg state $H_2(1/p)$ is p times that of ordinary H_2, the corresponding bond and vibrational energies are p^2 those of H_2, and the internuclear distance is

$$2c' = \frac{\sqrt{2}a_o}{p} \tag{6}$$

The experimental vibrational energy for the $\upsilon = 0$ to $\upsilon = 1$ transition of H_2 $E_{H_2(\upsilon=0\rightarrow\upsilon=1)}$ is [50-51]

$$E_{vib} = 0.515902\,eV \tag{7}$$

The vibrational energies E_{vib} for the $\upsilon = 0$ to $\upsilon = 1$ transition of hydrogen-type molecules $H_2(1/p)$ are [21, 40]

$$E_{vib} = p^2\,0.515902\,eV \tag{8}$$

where p is an integer. The experimental bond energy of the hydrogen molecule [52] is

$$E_D = 4.4783\,eV \tag{9}$$

The bond energies of hydrogen type-type molecules $H_2(1/p)$ are

$$E_D = p^2\,4.4783\,eV \tag{10}$$

For $H_2(1/2)$ with $p = 2$, the $\upsilon = 0$ to $\upsilon = 1$ vibrational transition energy and the bond energy are

$$E_{vib} = 2^2(0.515902)\,eV = 2.06361\,eV \tag{11}$$

and

$$E_D = 2^2(4.4783)\,eV = 17.913\,eV \tag{12}$$

respectively.

Typically, a third body is required to form hydrogen-type molecules. For example, the exothermic chemical reaction of $H+H$ to form H_2 does not occur with the emission of a photon. Rather, the reaction requires a collision with a third body, M, to remove the bond energy- $H+H+M \rightarrow H_2+M^*$ [1]. The third body distributes the energy from the exothermic reaction, and the end result is the H_2 molecule and an increase in the temperature of the system. However, in the case of the reaction to form $H_2(1/p)$ (Eq. (5)), radiation from a transition state that is resonant between the reacting hydrogen-type atoms and the molecule is possible. The transition state is equivalent to an excited state that is capable of radiating.

Ordinarily, $H_2(1/p)$ can not form an electronically excited radiative state; similarly, H_2 in its lowest state is nonradiative. However, both $H_2(1/p)$ and H_2 may radiate from excited vibrational states and absorb radiation to form excited vibrational states. During the reaction $2H(1/2) \rightarrow H_2(1/2)$ with $p=2$, H_2 is a resonant excited transition state. And, emission of the bond energy due to vibronic coupling is predicted with a resonance between the fundamental vibrational transition of H_2 ($\upsilon=0$ to $\upsilon=1$) and the corresponding transition of $H_2(1/2)$. The bond energy may be emitted with the energies of vibrational transitions in the transition state that superimpose to give emission to shorter or longer wavelengths of that corresponding to the bond energy. For a time harmonic oscillator, an integer number of wavelengths is resonant with the fundamental corresponding to reciprocal integer energies. Since the vibrational energy ($\upsilon=0$ to $\upsilon=1$ transition) increases by a factor of three with the formation of $H_2(1/2)$ compared to H_2 (the difference between Eqs. (11) and (7)), transitions are possible involving the formation of $H_2(1/2)$ in a excited vibrational state with the emission of the bond energy minus $\left(\frac{\upsilon^*}{3}\right)0.515902\,eV$. That is an energy of one third of an integer times the vibrational energy of H_2 goes to vibrational excitation, wherein $2 \le \upsilon^*$ corresponding to a first resonance of the transition state of $H_2(1/2)$ of least twice the vibrational energy of H_2. The energies E_{D+vib} of this red

series are given by

$$E_{D+vib} = p^2 E_{D H_2} - \left(\frac{\upsilon^*}{3}\right) E_{vib\, H_2(\upsilon=0\rightarrow\upsilon=1)} \quad , \quad \upsilon^* = 2,3... \qquad (13)$$
$$= 17.913 - \left(\frac{\upsilon^*}{3}\right) 0.515902\ eV$$

A violet series corresponds to transitions involving the formation of $H_2(1/2)$ with deexcitation from a vibrational state with the emission of the bond energy plus $\left(\frac{\upsilon^*}{3}\right) 0.515902\ eV$, one third of an integer times the vibrational energy of H_2. The energies E_{D+vib} of the violet series are given by

$$E_{D+vib} = p^2 E_{D H_2} + \left(\frac{\upsilon^*}{3}\right) E_{vib\, H_2(\upsilon=0\rightarrow\upsilon=1)} \quad , \quad \upsilon^* = 1,2,3... \qquad (14)$$
$$= 17.913 + \left(\frac{\upsilon^*}{3}\right) 0.515902\ eV$$

We report the results of microwave discharges of helium-hydrogen mixtures studied by EUV spectroscopy to search for line emission from transitions to fractional Rydberg states of atomic hydrogen. In addition, microwave discharges of neon-hydrogen and helium-hydrogen mixtures were studied by EUV spectroscopy to search for emission due to the formation of molecular hydrogen corresponding to fractional Rydberg states of atomic hydrogen. Since the electronic transitions and bond formation are very energetic the power balance was measured on a compound-hollow-cathode-glow discharge of a neon-hydrogen (99.5/0.5%) mixture.

II. Experimental

A. EUV spectroscopy

Spectra were obtained on hydrogen, helium, and xenon (not a catalyst in this system), mixtures of 2% hydrogen with helium or xenon and 0.5% hydrogen with neon. The noble gas-hydrogen mixtures were made from ultrahigh purity gases by addition of hydrogen to the noble gas to achieve the desired mixture based on the individual gas partial pressures.

For spectral measurement, the light emission from microwave

plasmas of hydrogen, helium, or neon alone, helium-hydrogen (98/2%), and neon-hydrogen (99.5/0.5%), and light emission from discharge plasmas of hydrogen alone was introduced to a normal incidence McPherson 0.2 meter monochromator (Model 302, Seya-Namioka type) equipped with a 1200 lines/mm holographic grating with a platinum coating. The wavelength region covered by the monochromator was $2-560\,nm$. The EUV spectrum was recorded with a channel electron multiplier (CEM) at $2500-3000\,V$ or a photomultiplier tube (PMT) at -1000 V and a sodium salicylate scintillator. The wavelength resolution was about $0.02\,nm$ (FWHM) with an entrance and exit slit width of $50\,\mu m$. The increment was $0.2\,nm$ and the dwell time was $500\,ms$. The PMT (Model R1527P, Hamamatsu) used has a spectral response in the range of $185-680\,nm$ with a peak efficiency at about $400\,nm$. The increment was $0.4\,nm$ and the dwell time was $1\,s$. Peak assignments were based on a calibration against the known He I, He II, Lyman series, Ne I, or Ne II lines.

To achieve higher sensitivity at the shorter EUV wavelengths, the light emission of control microwave plasmas of hydrogen, helium, and glow discharge plasmas of hydrogen, helium, xenon, helium-hydrogen (98/2%), and xenon-hydrogen (98/2%) were recorded with a McPherson 4° grazing incidence EUV spectrometer (Model 248/310G) equipped with a grating having 600 G/mm with a radius of curvature of $\approx 1\,m$. The angle of incidence was .87°. The wavelength region covered by the monochromator was $5-65\,nm$. The wavelength resolution was about $0.04\,nm$ (FWHM) with an entrance and exit slit width of $300\,\mu m$. The increment was $0.1\,nm$ and the dwell time was $500\,ms$. The light was detected by a CEM at $2400\,V$.

a. Microwave discharge emission spectra

The experimental set up comprising a microwave discharge gas cell light source and an EUV spectrometer which was differentially pumped is shown in Figure 1. EUV spectroscopy was recorded on hydrogen, helium, neon, xenon, helium-hydrogen (98/2%), neon-hydrogen (99.5/0.5%), and xenon-hydrogen (98/2%) microwave discharge plasmas (Frequency: 2450 MHz) according to the methods given previously [22]. Hydrogen, xenon,

helium, xenon-hydrogen (98/2%), or helium-hydrogen (98/2%) gas mixture was flowed at 1 Torr or 20 Torr through a half inch diameter quartz tube fitted with an Evenson cavity. Neon or neon-hydrogen (99.5/0.5%) gas mixture was flowed at about 300 mTorr except for a pressure variation study run at 200, 300, or 575 mTorr. The flow rate was about 10 sccm. With forced air cooling of the cell, the input power to the plasma was set at 85 W except for a helium control which was run with 100 W input. The light emission was recorded with an EUV spectrometer as described in Sec. IIA.

b. Glow discharge emission spectra

Extreme ultraviolet emission spectra were obtained on plasmas of hydrogen, helium, xenon, helium-hydrogen (98/2%), neon-hydrogen (95.5/0.5%), and xenon-hydrogen (98/2%) with a gas discharge cell that comprised a five-way stainless steel cross that served as the anode with a hollow stainless steel cathode. A diagram of the discharge plasma source is given in Figure 2. The experimental setup for the discharge measurements is illustrated in Figure 3. The cell comprised a five-way stainless steel cross that served as the anode with a hollow stainless steel cathode. The plasma was generated at the hollow cathode (0.5 cm ID) inside the discharge cell. The hollow cathode was constructed of a stainless steel rod inserted into a steel tube, and this assembly was inserted into an Alumina tube. The five-way cross was pressurized with 300-400 mTorr of gas which was maintained by flowing the gas while monitoring the pressure with a 1 Torr MKS Baratron absolute pressure gauge. The flow rate was about 10 sccm. An AC power supply (V = 0-1 kV, I = 0-100 mA) was connected to the hollow cathode to generate a discharge at the hollow cathode inside the discharge cell. The AC voltage and current at the time the EUV spectrum was recorded were 300-400 V and 40 mA, respectively. A Swagelok adapter at the very end of the steel cross provided a gas inlet and a connection with the pumping system, and the cell was pumped with a mechanical pump. Valves were between the cell and the mechanical pump, the cell and the monochromator, and the monochromator and its turbo pump. A flange opposite the end of the hollow cathode connected the spectrometer with

the cell. It had a small hole that permitted radiation to pass to the spectrometer. The hollow cathode and EUV spectrograph were aligned on a common optical axis using a laser. The light emission was recorded with a EUV spectrometer as described in Sec. IIA.

B. Power cell apparatus and procedure

Power balances were measured on plasmas with a catalyst, neon-hydrogen (99.5/0.5%) mixture, or a noncatalyst, xenon-hydrogen (98/2%) mixture. The plasmas were maintained in the cylindrical stainless steel gas cell shown in Figure 4 operated under flow conditions, and the power was measured by heat loss calorimetry as the input power was varied. The experimental setup for generating a glow discharge plasma and for measuring the power balance is shown in Figure 5. All experiments were performed in a kiln shown in Figure 5 maintained at a controlled constant temperature of $210.0 \pm 0.1°C$.

The 304-stainless steel cylindrical cell was 9.21 cm in diameter and 14.5 cm in height. The base of the cell contained a welded-in stainless steel thermocouple well (1 cm OD) which housed a thermocouple probe in the cell interior approximately 2 cm from the discharge and 2 cm from the cell axis. Also, a reentrant stainless steel tube (0.64 cm diameter) was at the base of the cell wall and was connected to a flexible stainless steel tube (100 cm in length) that served as a vacuum line from the cell. The top end of the cell was welded to a high vacuum 15.24 cm diameter conflat flange. A silver plated copper gasket was placed between a mating flange and the cell flange. The two flanges were clamped together with 10 circumferential bolts. The mating flange contained three penetrations comprising 1.) a stainless steel thermocouple well (1 cm OD) also housing a thermocouple probe in the cell interior approximately 2 cm from the discharge and 2 cm from the cell axis, 2.) a centered high voltage feedthrough which transmitted the power, supplied through a power connector, to a compound hollow cathode inside the cell, and 3.) a stainless steel reentrant tube (0.64 cm diameter and 100 cm in length) welded flush with the bottom surface of the top flange that served as the line to supply the test gas.

The diameter of the inlet and vacuum outlet were selected to be

0.64 cm which allowed for adequate flow while minimizing the formation of plasma in these tubes. In addition, the inlet and outlet tubes comprised reentrant tubes which extended significantly into the cell such that any plasma which formed in these tubes was contained within the cell. Thus, any heat which evolved due to plasma formation in these tubes was also contained in the cell.

The axial compound hollow cathode glow discharge electrode assembly shown in Figure 4 comprised a bundle of 19 tubes packed concentrically within a larger support tube and located adjacent to a planar anode disk. The bundled tubes were 316 stainless steel with outer diameter 0.953 cm, 0.89 mm wall thickness, and 5.1 cm length. A close-packed arrangement was used in which each interior tube in the bundle was surrounded by and was in contact with six neighboring tubes. The bundle was rigidly constructed by spot welding contacting tube pairs at the bundle ends. The 46 mm diameter tube bundle was fixed concentrically within the 48 mm ID stainless steel support tube by three set screws which passed radially through the support tube wall, making electrical contact with the bundle and support tube. The assembly was completed by a 316 stainless steel anode disk located concentrically within the support tube and oriented normal to the axis of the support tube/tube bundle assembly. The 42 mm diameter, 0.91 mm thick anode disk was electrically isolated from the support tube by a uniform annular gap of approximately 3 mm between the outer edge of the anode disk and the inner surface of the support tube. The anode disk and tube bundle end plane were separated by a distance of approximately 1 cm. The compound hollow cathode assembly consisting of the support tube, tube bundle, and anode disk was located on the axis of the cell. The tube bundle, support tube and cell body were maintained at ground potential while voltage for the anode disk was supplied by the high voltage feed-through on the cell upper flange.

A 1.6 mm thick UV-grade sapphire window with 1.5 cm view diameter provided a visible light path from inside the cell to monitor the plasma. The viewing direction was normal to the cell axis. An 8 mm quartz rod channeled the light from the view port through a stainless tube to a collimating lens which was focused on a 100 μm optical fiber located outside the furnace. Spectral data was recorded with a visible

spectrometer and stored by a personal computer.

The cell was evacuated with a turbo vacuum pump to a pressure of <1 mTorr. The gas in each experiment was ultrahigh purity grade or higher. The gas pressure inside the cell was maintained at 1 Torr with a neon gas flow rate of 40 sccm and a hydrogen flow rate of 0.2 sccm or a xenon flow rate of 40 sccm and a hydrogen flow rate of 0.8 sccm. Each gas flow was controlled by a mass flow controller. The cell pressure was monitored by an absolute pressure gauge.

The discharge was started and maintained by a DC electric field in the compound hollow cathode supplied by a constant voltage DC power supply (Xantrex XRF 600-2). The input power was calculated as the product of the constant voltage times the current. The voltage between the cathode and anode was monitored by a digital multimeter (Digital Instruments 9300GB). A duplicate multimeter in series with the discharge gap was used to indicate the current. The power was increased by ramping the constant voltage.

C. Power balance measurements

The temperature response of the cell to input power for the test and control gas mixtures was determined. The temperature at the two thermocouples was recorded and averaged about one hour after the cell had reached a thermal steady state. The time to reach a steady state temperature with each increase in the input power to the glow discharge was typically 3-4 hours. At this point, the power Q lost from the cell was equal to the power supplied to the cell Q_{in} plus any excess power Q_{gen}.

$$Q = Q_{in} + Q_{gen} \tag{15}$$

The rate of heat loss from the cell was of the form

$$Q = a(T - T_0) + b(T^4 - T_0^4) \tag{16}$$

where T was the cell temperature, $T_0 = 210.0\ ^\circ C = 483.2\ K$ was the fixed kiln temperature, and a and b are parameters. The first term on the right corresponds to heat loss by conduction and convection, and the second term corresponds to radiation heat loss. Expanding and rearranging results in

$$Q = (a + 4bT_0^3)\Delta T + b\left[6(T_0\Delta T)^2 + 4T_0\Delta T^3 + \Delta T^4\right] \tag{17}$$

where $\Delta T = T - T_0$ is the cell temperature rise above the kiln temperature. Because xenon plasma is a control, the rate of heat loss from the cell in the case of a xenon-hydrogen (98/2%) plasma was identical to the measured electrical power input ($Q_{gen} = 0$).

ΔT was recorded as a function of input power Q_{in} for noncatalyst xenon with hydrogen over the input power range of 65 to 400 W. The higher temperature produced by the neon-hydrogen plasmas compared with the xenon-hydrogen plasma was representative of the excess power since the cell temperature rise was found to be insensitive to heat transfer mechanisms occurring inside of the cell—the transfer to the cell walls being very fast and heat loss from the wall to the outside ambient environment dominating the cell temperature. In the case of each catalyst run, the total output power Q was determined by solving Eq. (17) using the measured ΔT. The excess power Q_{gen} was determined from Eq. (15).

III. Results and discussion

A. EUV Spectroscopy

a. Detection of fractional Rydberg state atomic hydrogen

In the case of the EUV spectra of hydrogen, xenon, or xenon-hydrogen (98/2%), no peaks were observed below 80 nm, and no spurious peaks or artifacts due to the grating or the spectrometer were observed. Only known He I and He II peaks were observed in the EUV spectrum of the control helium microwave discharge cell emission. The helium glow discharge emission was equivalent to the helium microwave emission.

The EUV spectra ($17.5 - 50\ nm$) of the microwave cell emission of the helium-hydrogen (98/2%) mixture (top curve) and the helium control (bottom curve) are shown in Figure 6. Ordinary hydrogen has no emission in these regions. Novel peaks were observed at $45.6\ nm$, $37.4\ nm$, and $20.5\ nm$ which do not correspond to helium. At the 1 Torr condition, additional novel peaks were observed in the short wavelength region ($5 - 65\ nm$) at $14.15\ nm$, $13.03\ nm$, $10.13\ nm$, and $8.29\ nm$ which do not

correspond to helium as shown in Figure 7. Known He I lines which were used for calibration of the novel peak positions were observed at $58.4\,nm$, $53.7\,nm$, and $52.4\,nm$. It is proposed that the $30.4\,nm$ peak shown in Figures 6 and 7 was not entirely due to the He II transition. In the case of the helium-hydrogen mixture, the ratio of the $30.4\,nm$ ($40.8\,eV$) peak intensity to the $25.6\,nm$ ($48.3\,eV$) peak intensity was 10 compared to 5.4 for helium alone as shown in Figure 6. This implies only a minor contribution to the $30.4\,nm$ peak from the He II transition.

It is proposed that the majority of the $91.2\,nm$ peak that we observed was also due to a novel transition. At 20 Torr, the ratio of the Lyman β peak intensity to that of the $91.2\,nm$ peak of the helium-hydrogen plasma was 2 compared to 8 for each control hydrogen and xenon-hydrogen plasma. This indicates that the majority of the $91.2\,nm$ peak was due to a transition other than the binding of an electron by a proton.

The novel peaks fit two empirical relationships. In order of energy, the set comprising the peaks at $91.2\,nm$, $45.6\,nm$, $30.4\,nm$, $13.03\,nm$, $10.13\,nm$, and $8.29\,nm$ correspond to energies of $q \cdot 13.6\,eV$ where $q = 1,2,3,7,9,11$. In order of energy, the set comprising the peaks at $37.4\,nm$, $20.5\,nm$, and $14.15\,nm$ correspond to energies of $q \cdot 13.6 - 21.21\,eV$ where $q = 4,6,8$. These lines can be explained as electronic transitions to fractional Rydberg states of atomic hydrogen given by Eqs. (2a) and (2c) wherein the catalytic system involves helium ions because the second ionization energy of helium is $54.417\,eV$, which is equivalent to $2 \cdot 27.2\,eV$. In this case, $54.417\,eV$ is transferred nonradiatively from atomic hydrogen to He^+ which is resonantly ionized. The electron decays to the $n = 1/3$ state with the further release of $54.417\,eV$ which may be emitted as a photon. The catalysis reaction is

$$54.417\,eV + He^+ + H[a_H] \rightarrow He^{2+} + e^- + H\left[\frac{a_H}{3}\right] + 108.8\,eV \tag{18}$$

$$He^{2+} + e^- \rightarrow He^+ + 54.417\,eV \tag{19}$$

And, the overall reaction is

$$H[a_H] \rightarrow H\left[\frac{a_H}{3}\right] + 54.4\,eV + 54.4\,eV \tag{20}$$

Since the products of the catalysis reaction have binding energies of $m \cdot 27.2\,eV$, they may further serve as catalysts. Thus, further catalytic

transitions may occur: $n=\frac{1}{3}\rightarrow\frac{1}{4}$, $\frac{1}{4}\rightarrow\frac{1}{5}$, and so on.

Electronic transitions to Rydberg states given by Eqs. (2a) and (2c) catalyzed by the resonant nonradiative transfer of $m\cdot 27.2\,eV$ would give rise to a series of emission lines of energies $q\cdot 13.6\,eV$ where q is an integer. It is further proposed that the photons that arise from hydrogen transitions may undergo inelastic helium scattering. That is, the catalytic reaction

$$H[a_H]\xrightarrow{He^+}H\left[\frac{a_H}{3}\right]+54.4\,eV+54.4\,eV \tag{21}$$

yields $54.4\,eV$ by Eq. (19) and a photon of $54.4\,eV$ ($22.8\,nm$). Once emitted, the photon may be absorbed or scattered. When this photon strikes $He(1s^2)$, $21.2\,eV$ may be absorbed in the excitation to $He(1s^1 2p^1)$. This leaves a $33.19\,eV$ ($37.4\,nm$) photon peak and a $21.2\,eV$ ($58.4\,nm$) photon from $He(1s^1 2p^1)$. Thus, for helium the inelastic scattered peak of $54.4\,eV$ photons from Eq. (18) is given by

$$E=54.4\,eV-21.21\,eV=33.19\,eV\ (37.4\,nm) \tag{22}$$

A novel peak shown in Figures 6 and 7 was observed at $37.4\,nm$. Furthermore, the intensity of the $58.4\,nm$ peak corresponding to the spectra shown in Figure 7 was about 60,000 photons/sec. Thus, the transition $He(1s^2)\rightarrow He(1s^1 2p^1)$ dominated the inelastic scattering of EUV peaks. The general reaction is

$$photon\,(h\nu)+He\,(1s^2)\rightarrow He\,(1s^1 2p^1)+photon\,(h\nu-21.21\,eV) \tag{23}$$

The two empirical series may be combined—one directly from Eqs. (2a, 2c) and the other indirectly with Eq. (23). The energies for the novel lines in order of energy are $13.6\,eV$, $27.2\,eV$, $40.8\,eV$, $54.4\,eV$, $81.6\,eV$, $95.2\,eV$, $108.8\,eV$, $122.4\,eV$ and $149.6\,eV$. The corresponding peaks are $91.2\,nm$, $45.6\,nm$, $30.4\,nm$, $37.4\,nm$, $20.5\,nm$, $13.03\,nm$, $14.15\,nm$, $10.13\,nm$, and $8.29\,nm$, respectively. Thus, the identified novel lines correspond to energies of $q\cdot 13.6\,eV$ where $q=1,2,3,4,6,7,8,9,11$ or these lines inelastically scattered by helium atoms wherein $21.2\,eV$ was absorbed in the excitation of $He(1s^2)$ to $He(1s^1 2p^1)$. The values of q observed are consistent with those excepted based on Eq. (20) and the subsequent autocatalyzed reactions as discussed previously [22]. The satellite peak at $44.2\,nm$ shown in Figures 6 and 7 may be due to multipole coupling as discussed elsewhere [14]. The broad line width of the $H(1/p)$ lines is consistent with the expected

very short lifetime of the corresponding emitting energetic intermediates formed by the nonradiative energy transfer. The observation in Figure 6 that the $30.4\,nm$ is broader than that of the control further supports the assignment given in Table I discussed previously. There is remarkable agreement between the data and the proposed transitions to fractional Rydberg states and these lines inelastically scattered by helium according to Eq. (23). Additional lines were observed in the region 60-100 nm which were assigned to the lower energy hydrogen molecule $H_2(1/2)$ as discussed in Sec. IIIAb. All other peaks could be assigned to He I, He II, second order lines, or atomic or molecular hydrogen emission. No known lines of helium or hydrogen explain the $q \cdot 13.6\,eV$ related set of peaks.

The catalysis reaction of atomic hydrogen to form atoms in fractional Rydberg states is exothermic based on the observed $q \cdot 13.6\,eV$ emission. And, the substantial intensity of the $q \cdot 13.6\,eV$ peaks, despite the very low grating efficiency at these short wavelengths, implied appreciable reaction rates corresponding to significant power generation. An estimate of the power of the helium-hydrogen microwave plasma was reported previously [15]. It was maintained under conditions matching those given in Sec. II except that the constant input power was 40 W rather than 85. The power estimate based on the rise of the neutral gas temperature confirmed that substantial power was released. With a microwave input power of $40\,W$, no increase in temperature was observed with the addition of hydrogen to xenon control. In contrast, the plasma gas temperature increased from room temperature to 1200°C within 150 seconds for helium-hydrogen compared to only 185°C for helium alone. A conservative estimate of the total output power was determined to be $400\,W$. Since the hydrogen flow rate was 1 sccm, an estimate of the corresponding energy balance was over $-5\,X\,10^5\,kJ/mole\,H_2$ compared to the enthalpy of combustion of hydrogen of $-241.8\,kJ/mole\,H_2$. The power balance of a glow discharge neon-hydrogen plasma is discussed in Sec. IIB.

b. Detection of fractional Rydberg state molecular hydrogen

The EUV emission was recorded from microwave and glow discharge plasmas of 1.) hydrogen, helium, neon, and xenon alone, 2.)

xenon and helium with 2% hydrogen, and 3.) neon with 0.5% hydrogen over the wavelength range 5-125 nm. The EUV spectrum (20-125 nm) of the control hydrogen discharge cell emission is shown in Figure 8. The hydrogen glow discharge and microwave discharge emission recorded with the normal incidence monochrometer and the 4° grazing EUV spectrometer were the same. The EUV spectra (20-50 nm) and (40-100 nm) of the control xenon (top curve), control xenon-hydrogen (98/2%) mixture (middle curve), and control hydrogen (bottom curve) glow discharge cell emission are shown in Figures 9 and 10, respectively. No peaks were observed in these controls except hydrogen peaks for wavelengths greater than about 85 nm. Thus, xenon did not catalyze hydrogen to give novel peaks, and no spurious peaks or artifacts due to the grating or the spectrometer were observed. The EUV spectrum (20-100 nm) of the control helium microwave cell emission is shown in Figure 11. Only known He I and He II peaks were observed.

The EUV spectrum (5-100 nm) of the microwave cell emission of the helium-hydrogen (98/2%) mixture is shown in Figure 12. Reproducible novel emission lines were observed at 45.6 *nm*, 30.4 *nm*, and 8.29 *nm* with energies of $q \cdot 13.6\,eV$ where $q = 2,3,\ or\ 11$ and at 37.4 *nm*, and 20.5 *nm* with energies of $q \cdot 13.6\,eV$ where $q = 4\ or\ 6$ that were inelastically scattered by helium atoms wherein 21.2 *eV* was absorbed in the excitation of $He\,(1s^2)$ to $He\,(1s^1 2p^1)$ as proposed in Eq. (23). In addition, a series of peaks were observed in the 60-100 nm region of Figure 12. They do not match helium as shown in Figures 6 and 11. The wavelength-labeled peaks in Figure 12 match members of peaks predicted at $E_{D+vib} = 17.913 \pm \left(\frac{\upsilon^*}{3}\right) 0.515902\,eV, \quad \upsilon^* = 1,2,3...$ due to the reaction $2H(1/2) \rightarrow H_2(1/2)$ with vibronic coupling. The peaks assigned in Table 1 corresponded to members of the longer wavelengths series $\upsilon^* = 2$ to $\upsilon^* = 32$ (Eq. (13)) and the shorter wavelength series $\upsilon^* = 1$ to $\upsilon^* = 16$ (Eq. (14)). Hydrogen has no peaks short of 80 nm. To distinguish the wavelength-labeled peaks due to $H_2(1/2)$ formation from hydrogen peaks, the overlay of the spectra (60-100 nm) of the microwave cell emission of a helium-hydrogen (98/2%) plasma and the hydrogen plasma are shown in Figure 13. The spectra were aligned using the hydrogen L_γ line at 97.25 nm. The peaks due to $H_2(1/2)$ formation are assigned in Table 1

based on the continuation of Eq. (13) to longer wavelengths. The position of these predicted peaks matched peaks in the helium-hydrogen spectrum. In many cases, the hydrogen spectrum does not have peaks at the positions of the peaks that are wavelength-labeled in the figures and assigned to $H_2(1/2)$ formation in Table 1. In other cases, the distinction from molecular hydrogen requires further scrutiny. For example, both the helium-hydrogen and the hydrogen plasmas have peaks at the position of L_γ line at 97.25 nm and at 88.8 nm. The 97.25 peak requires addition study. However, the 88.8 nm peak of the helium-hydrogen plasma is narrower than the corresponding hydrogen peak and has a much greater intensity when the hydrogen peak is normalized to the other peaks of the hydrogen spectrum. Deuterium substitution studies are being pursued to firmly identify any overlapping peaks.

The peaks of helium in this region are He I at 50.5500, 50.5684, 50.5912, 50.62000, 50.65702, 50.70576, 50.77178, 50.86431, 50.99980, 51.20983, 51.56166, 52.22128, 53.70296, 58.43340, and 59.1412 nm and He II at 95.870, 97.211, and 99.236 nm [53]. The helium plasma was much weaker in the absence of 2% hydrogen. The observed helium peaks are identified in Figure 12. Helium does not have peaks at the positions of the wavelength-labeled peaks assigned to $H_2(1/2)$ formation in Table 1 except for He II at 95.870, and 97.211 which are close to the $\upsilon^* = 29$ red series peak predicted at 95.918 nm and the $\upsilon^* = 30$ red series peak predicted at 97.211 nm, respectively. Deuterium substitution studies are being pursued to firmly identify these overlapping peaks.

The three EUV spectra (48-65 nm) of the glow discharge cell emission of the helium-hydrogen (98/2%) plasma are shown in Figure 14. The EUV spectrum (50-65 nm) of the control helium microwave discharge cell emission is shown in Figure 15. The control plasma was run at 20 Torr with 100 W input to the plasma to increase the intensity of the lines. The spectrum was recorded with a normal incidence EUV spectrometer which has less sensitivity but also less noise and a higher resolution than the grazing incidence spectrometer. Only known He I peaks were observed. The novel series of wavelength-labeled peaks observed in the 60-65 nm region of Figure 14 were assigned to members of peaks predicted at $E_{D+vb} = 17.913 + \left(\frac{\upsilon^*}{3}\right) 0.515902\, eV$ due to the reaction

$2H(1/2) \rightarrow H_2(1/2)$ with vibronic coupling. The peaks assigned in Table 1 corresponded to members of the violet series with $\upsilon^* = 8$ to $\upsilon^* = 16$. The agreement of the data with predictions was within about ± 0.15 nm which was the resolution of the 4° grazing incidence spectrometer. The helium peaks matched within this level of resolution also. These results demonstrate the formation of $H_2(1/2)$ in a glow discharge plasma reaction as well as in microwave plasmas. The assignment of the lines in the 60-65 nm region of Figure 14 to members of the violet series given by Eq. (14) resolves the problem faced by the authors previously [22]. These lines were observed in a helium-hydrogen plasma in a region where ordinary hydrogen does not emit, and the lines did not appear in the NIST tables [53].

The novel series of peaks due to $H_2(1/2)$ formation in helium hydrogen (98/2%) microwave plasmas were repeatable as shown in Figure 16. An additional two EUV spectra (45-100 nm) of the microwave cell emission of the helium-hydrogen (98/2%) plasma that showed peaks equivalent to those shown in Figures 12-14, 16 are shown in Figure 17 and 18. All of the peaks identified in Table 1 were identified over various runs; however, variations in intensities of the peaks were observed between different runs and the same run obtained at different times. These differences were found to be dependent on reaction conditions such as pressure, and they may also be due to temporal variations in plasma parameters such as the plasma thermal neutral temperature. Another likely important factor is variations in concentrations of reactants such as $H(1/2)$ due to changes in the catalysis reaction rate or due to competing reactions for $H(1/2)$ such as hydride ion formation [8, 11-12, 18, 23, 26], autocatalysis reactions [22], or the formation of novel hydride compounds such as $SiH(1/p)$ [5].

Furthermore, some peaks were consistently much less intense than others. For example, the red series $\upsilon^* = 9$ peak at 75.75 nm corresponds to three times the vibrational energy of H_2 and was very weak or absent in many cases. Vibronic coupling at integer multiples of the vibrational energy of H_2 compared to thirds may be partially forbidden. This may be due to an extended transition-state lifetime which can not de-excite by emission before the state decays back to the reactants, $H(1/2)$.

Figure 19 is the EUV spectrum (62.5-100 nm) of the microwave cell

emission of a helium-hydrogen (98/2%) plasma which showed the $q \cdot 13.6\,eV$ series of peaks in the 5-50 nm region that was equivalent to that shown in Figure 12. Peaks of the $E_{D+vib} = 17.913 \pm \left(\frac{\upsilon^*}{3}\right) 0.5159\,eV$ series about the position of the $H_2(1/2)$ bond energy of 69.214 nm were observed. It is apparent from Figures 17-19 that the series of peaks due to vibronic coupling is centered about the $H_2(1/2)$ bond energy of 17.913 eV given by Eqs. (13) and (14). As shown in Figure 19 and Table 1, the red series started with $\upsilon^* = 2$, and the violet series started with $\upsilon^* = 1$ corresponding to the peaks at 70.60 and 68.60 nm, respectively. Thus, the corresponding minimum energy for vibronic coupling with the formation of a resonant excited molecular state was 2/3 the vibrational energy of H_2, and the minimum energy released in addition to the bond energy was equivalent to 1/3 the vibrational energy of H_2.

The frequency for vibration is much greater than that for rotation. Thus, the time constant for vibronic coupling should be shorter, and vibronic coupling should be the predominant mechanism that permits the bond energy of $H_2(1/2)$ to be emitted. The peaks due to vibronic coupling are assigned in Figures 12-14 and 16-19 and Table 1. However, it is proposed that rotational coupling as well as vibrational coupling may occur during the reaction $2H(1/2) \rightarrow H_2(1/2)$.

The experimental rotational energy E_{rot} emitted by a hydrogen-type molecule with the transition from the state with the rotational quantum number $J+1$ to one with the rotational quantum number J is [54]

$$E_{rot} = (J+1)1.47\,X\,10^{-2}\,eV \tag{24}$$

The rotational energy for the $J+1$ to J transition of hydrogen-type molecules $H_2(1/p)$ is [21, 40]

$$E_{rot} = p^2(J+1)1.47\,X\,10^{-2}\,eV \tag{25}$$

where p is an integer. For $H_2(1/2)$ with $p=2$, the $J+1$ to J rotational transition energy is

$$E_{rot} = 2^2(J+1)1.47\,X\,10^{-2}\,eV = (J+1)5.88\,X\,10^{-2}\,eV \tag{26}$$

The $\upsilon^* = 2$ violet series peak at 67.90 nm was split into another peak to the violet at 67.70 nm. The 0.054 eV separation of these peaks matches the rotational energy of $H_2(1/2)$ for the $J=1$ to $J=0$ transition. In this case, the energy of the reaction $2H(1/2) \rightarrow H_2(1/2)$ was released by vibration-rotational coupling to give the additional 67.70 nm peak. Many

of the peaks of Figure 19 show rotational features shifted by about 0.06 eV such as the $\upsilon^* = 7$ red series peak at 74.20 nm with the violet shifted peak at 73.95 and the $\upsilon^* = 13$ red series peak at 79.10 nm with a violet shifted peak at 78.80 nm. Addition examples can be found in Figures 12 and 13 such as the $\upsilon^* = 31$ red series peak shown at 98.50 nm with the violet shifted peak at 98.05 nm and the $\upsilon^* = 27$ red series peak at 93.45 nm with a violet shifted peak at 93.00 nm. Some of the more prominent rotational peaks are shown in the figures in smaller font.

Figure 19 shows the most complete spectra containing essentially all of the peaks given in Table 1 as well as rotational peaks. The high pressure condition of 20 Torr was run to obtain the data of Figure 19; otherwise, the plasma was maintained at 1 Torr. These results indicate that the formation of $H_2(1/2)$ is favored at higher pressure. Figure 20 shows the plot of the theoretical emission vacuum wavelengths E_{DH_2} due to the reaction $2H(1/2) \rightarrow H_2(1/2)$ with vibronic coupling at energies of $E_{D+vib} = p^2 E_{DH_2} \pm \left(\frac{\upsilon^*}{3}\right) E_{vib\,H_2(\upsilon=0\rightarrow\upsilon=1)}$ $(p = 2)$ and the wavelengths observed as shown in Figures 12-14 and 16-19 and given in Table 1. The data matched to longer wavelengths for $\upsilon^* = 2$ to $\upsilon^* = 32$ (Eq. 13)) and to shorter wavelengths for $\upsilon^* = 1$ to $\upsilon^* = 16$ (Eq. (14)) to within the spectrometer resolution of about ±0.05%.

The series of vibrational peaks from the helium-hydrogen plasmas shown in Figures 12-14 and 16-19 were also observed with the neon catalyst only with hydrogen. The EUV spectrum (20-100 nm) of the control neon microwave discharge cell emission is shown in Figure 21. The plasma was much less intense without hydrogen, and only known Ne I peaks were observed. The EUV spectrum (50-100 nm) of the microwave cell emission of the neon-hydrogen (99.5/0.5%) mixture is shown in Figure 22. The novel series of wavelength-labeled peaks was observed that was assigned to members of peaks predicted at $E_{D+vib} = 17.913 \pm \left(\frac{\upsilon^*}{3}\right) 0.515902\, eV$ due to the reaction $2H(1/2) \rightarrow H_2(1/2)$ with vibronic coupling. The peaks assigned in Table 1 corresponded to members of the longer wavelength series $\upsilon^* = 2$ to $\upsilon^* = 32$ and the shorter wavelength series $\upsilon^* = 1$ to $\upsilon^* = 16$. The neon catalyst reaction to form $H_2(1/2)$ was reproducible. The EUV spectrum (55-100 nm) of a

replication of the microwave cell emission from a neon-hydrogen (99.5/0.5%) plasma is shown in Figure 23, and the 55-85 nm region of Figure 23 is shown in Figure 24. The observed peaks assigned in Table 1 were equivalent to those shown in Figure 22.

The effect of the variation of the gas pressure was determined as shown in Figure 25. Based on the presence of the novel series of peaks which were equivalent to those shown in Figures 22-24, the neon catalyst reaction showed slight pressure dependence over the range of 200-575 mTorr. In contrast, continuum peaks to shorter and to longer wavelengths were only observed as the pressure was increased from 200 to 575 mTorr. The identity of the continua is discussed in Sec. IIIC.

B. Power balance measurements

The plot of the discharge cell temperature increase above the constant kiln temperature of $210.0 \pm 0.1\,^{\circ}C$ as a function of the power applied to the gas mixtures at 1 Torr total pressure is shown in Figure 26. The temperature response with xenon-hydrogen (98/2%) was plotted over a broader range (65 W to 400 W) than that for neon-hydrogen (99.5/0.5%) (100-350 W) in order to generate a calibration curve which better corresponded to the higher temperatures achieved with the neon-hydrogen mixture. Fitting the parameters a and b of Eq. (17) to the ΔT and Q_{in} data for xenon-hydrogen plasma given in Table 2 yielded

$$Q = (1.445\ W/K)\Delta T + (4.779\ X\ 10^{-9}\ W/K^4)\left[6(T_0\Delta T)^2 + 4T_0\Delta T^3 + \Delta T^4\right] \qquad (27)$$

with an rms deviation of the data from the curve fit of 5.0 W, cf. Figure 26. The power generated by the neon-hydrogen (99.5/0.5%) plasma corresponding to a cell temperature rise ΔT is the difference between the rate of heat loss from the cell and the measured power input $Q_{Ne/H_2}(\Delta T)$:

$$Q_{gen}(\Delta T) = Q(\Delta T) - Q_{Ne/H_2}(\Delta T) \qquad (28)$$

Power generation for the neon-hydrogen plasma is given in Table 3. For a power input to the glow discharge of 350 W, the excess output power was $306 \pm 5\ W$ based on a comparison of the temperature rise of the cell with neon-hydrogen (99.5/0.5%) mixture and xenon-hydrogen (98/2%) mixture. As shown in Figure 26 and Table 3, the excess power increased disproportionately with increasing input power. Since the hydrogen flow rate was 0.2 sccm, an estimate of the corresponding energy balance at

306 W excess power was over $-1 X 10^6\ kJ/mole\ H_2$ compared to the enthalpy of combustion of hydrogen of $-241.8\ kJ/mole\ H_2$. The results were found to be repeatable in separate experiments.

C. Neon catalyst mechanism

Neon is exceptional in that several catalyst mechanisms are possible. A neon ion and a proton can provide a net enthalpy of $m \cdot 27.2\ eV$, a multiple of that of the potential energy of the hydrogen atom. The second ionization energy of neon is $40.96\ eV$, and H^+ releases $13.6\ eV$ when it is reduced to H. The combination of reactions of Ne^+ to Ne^{2+} and H^+ to H, then, has a net enthalpy of reaction of $27.36\ eV$, which is equivalent to $m = 1$. The balanced reaction is

$$27.36\ eV + Ne^+ + H^+ + H\left[\frac{a_H}{p}\right] \rightarrow H + Ne^{2+} + H\left[\frac{a_H}{(p+1)}\right] + [(p+1)^2 - p^2] X 13.6\ eV \quad (29)$$

$$H + Ne^{2+} \rightarrow H^+ + Ne^+ + 27.36\ eV \quad (30)$$

And, the overall reaction is

$$H\left[\frac{a_H}{p}\right] \rightarrow H\left[\frac{a_H}{(p+1)}\right] + [(p+1)^2 - p^2] X 13.6\ eV \quad (31)$$

The lines of Ne^+, and Ne^{2+} corresponding to the catalytic reaction given by Eqs. (29-31) were observed on a glow discharge at a hollow cathode described in Sec. IIAb. A compound hollow cathode was used in the power balance measurements as described in Sec. IIB. The assignments of the peaks shown in Figure 27 were confirmed by NIST tables [53, 55]. Ne^{2+} was observed at 49.1, 37.9, 32.8, 31.3, 30.8, 30.1, 28.4, and 26.7 nm. Ne^+ was observed at 46.07, 44.7, 40.7, 36.24, 35.7, 35.4, 33.1, and 32.8 nm.

The first neon excimer continuum Ne_2^* may also provide a net enthalpy that is a multiple of that of the potential energy of the hydrogen atom. The first ionization energy of neon is $21.56454\ eV$ [56], and the first neon excimer continuum Ne_2^* has an excited state energy in the region of $15.92\ eV$ [57]. The combination of reactions of Ne_2^* to $2Ne^+$, then, has a net enthalpy of reaction of $27.21\ eV$, which is equivalent to $m = 1$. The balanced reaction is

$$27.21\ eV + Ne_2^* + H\left[\frac{a_H}{p}\right] \rightarrow 2Ne^+ + H\left[\frac{a_H}{(p+1)}\right] + [(p+1)^2 - p^2] X 13.6\ eV \quad (32)$$

$$2Ne^{+} \rightarrow Ne_2^{*} + 27.21\ eV \tag{33}$$

And, the overall reaction is

$$H\left[\frac{a_H}{p}\right] \rightarrow H\left[\frac{a_H}{(p+1)}\right] + [(p+1)^2 - p^2]X13.6\ eV \tag{34}$$

The series of peaks shown in Figure 22 were assigned in Table 1 to the reaction $2H(1/2) \rightarrow H_2(1/2)$. These peaks were observed on top of a broad continuum in the 77.5 nm region that was assigned to the 1st neon excimer continuum peak [57]. The first neon excimer continuum is also shown in Figure 25 as distinct from other peaks in this region by a high resolution spectrum (slit widths of $20\ \mu m$) and by the increase in its intensity with neon pressure.

The observation of the neon excimer with continuum emission at the ionization edge of *Ne* also shown in Figure 25 that increased as the pressure was increased from 200 mTorr to 575 mTorr supports the possibility that the neon excimer serves as a catalyst (Eqs. (32-34)). Similar emission by catalysts at their ionization edge with the formation of lower-energy hydrogen products has been reported previously [26].

Cesium atoms ionize at an integer multiple of the potential energy of atomic hydrogen, $m \cdot 27.2\ eV$. The enthalpy of ionization of *Cs* to Cs^{2+} has a net enthalpy of reaction of $27.05135\ eV$, which is equivalent to $m = 1$ [56]. And, the reaction Ar^{+} to Ar^{2+} has a net enthalpy of reaction of $27.63\ eV$, which is equivalent to $m = 1$ [56]. Emission was observed from a continuum state of Cs^{2+} and Ar^{2+} at $53.3\ nm$ and $45.6\ nm$, respectively [26] corresponding to the deexcitation following the resonant energy transfer. The single emission feature with the absence of the other corresponding Rydberg series of lines from these species confirmed the resonant nonradiative energy transfer of $27.2\ eV$ from atomic hydrogen to atomic cesium or Ar^{+}. The product $H(1/2)$ reacted to form the hydride ion $H^{-}(1/2)$ as shown by the emission observed at $407\ nm$ corresponding to its predicted binding energy of $3.05\ eV$.

Neon serves as a catalyst to form $H_2(1/2)$ as well as substantial heat. However, it has been reported previously that there was no Balmer α line broadening with neon as catalyst, whereas, significant broadening was observed for all atoms and ions capable of providing a reaction with a net enthalpy of $m \cdot 27.2\ eV$ [4, 7-8, 11, 13-17, 20, 30, 34]. From the width of the 656.3 nm Balmer α line emitted from microwave and glow

discharge plasmas, it was found that a strontium-hydrogen microwave plasma showed a broadening similar to that observed in the glow discharge cell of $27\text{-}33\,eV$; whereas, in both sources, no broadening was observed for control magnesium-hydrogen. Microwave helium-hydrogen and argon-hydrogen plasmas showed extraordinary broadening corresponding to an average hydrogen atom temperature of $180\text{-}210\,eV$ and $110\text{-}130\,eV$, respectively. The corresponding results from the glow discharge plasmas were $33\text{-}38\,eV$ and $30\text{-}35\,eV$, respectively, compared to $\approx 4\,eV$ for plasmas of pure hydrogen, neon-hydrogen, krypton-hydrogen, and xenon-hydrogen maintained in either source [13].

The explanation of the absence of Balmer α line broadening may be that hydrogen transfers the entire energy of the transition (Eqs. (2a) and (2c)) to neon catalyst without forming an excited intermediate as is the case with other catalysts which accept $m \cdot 27.2\,eV$ from atomic hydrogen. In the latter case, the line broadening as well as the further observation of an inverted population in some cases [4] is explained by a resonance nonradiative energy transfer from the short-lived highly energetic intermediates. That is atoms undergoing catalyzed transitions to states given by Eqs. (2a) and (2c), yield $H(n>2)$ atoms directly by multipole coupling [14] and fast $H(n=1)$ atoms. The emission of $H(n=3)$ from fast $H(n=1)$ atoms excited by collisions with the background H_2 has been discussed by Radovanov et al. [58].

The catalysis of $H(1)$ to $H(1/2)$ releases $40.8\,eV$, and the second ionization energy of neon is 40.96328 [56]. Ne^+ may absorb about $40.8\,eV$ and ionize to Ne^{2+} which is resonant with the difference in energy between the $p=2$ and the $p=1$ states of atomic hydrogen given by Eqs. (2a) and (2c). Thus, Ne^+ may serve as a catalyst to cause the transition between these hydrogen states. The catalysis reaction is

$$40.96328\,eV + Ne^+ + H\left[\frac{a_H}{p}\right] \rightarrow Ne^{2+} + H\left[\frac{a_H}{(p+1)}\right] + [(p+1)^2 - p^2]X13.6\,eV \tag{35}$$

$$Ne^{2+} \rightarrow Ne^+ + 40.96328\,eV \tag{36}$$

And, the overall reaction is

$$H\left[\frac{a_H}{p}\right] \rightarrow H\left[\frac{a_H}{(p+1)}\right] + [(p+1)^2 - p^2]X13.6\,eV \tag{37}$$

The mechanism given by Eqs. (35-37) does not provide an energetic short-lived intermediate to give rise to line broadening. Further support

is provided by the observation of an elevated electron temperature with neon as the catalyst [13].

It was observed previously that the catalysis with Ar^+ was optimal with an argon-hydrogen mixture in the range of 97-95% argon with 3-5% hydrogen, respectively [26-27]. Other catalysts such as *Cs*, *K*, *Sr* and Rb^+ were run with pure hydrogen [35]. Neon was found to be exceptionally sensitive to the hydrogen concentration. For concentrations much above 1%, no power or novel spectral lines were observed. A possible explanation is that the reaction depends on hydrogen and catalyst that was removed by excess hydrogen. The neon excimer may be removed by excess hydrogen. Or, the reaction may depend on Ne^+ as well as atomic hydrogen, but atomic and molecular hydrogen reduce Ne^+. Another possibility is that the catalysis reaction depends on H^+ and Ne^+ according to Eqs. (29-31). In this case, the H^+ concentration is strongly dependent on the H_2 concentration due to the reaction

$$H^+ + H_2 \rightarrow H_3^+ \tag{38}$$

In the low pressure range, the H^+ concentration can decrease by an order of magnitude upon doubling the H_2 pressure as shown by Chen, Collins, and Phillips [59].

Relationships between power release, the formation of $H_2(1/2)$, and the intensity and energy of the catalyst species are being further studied spectroscopically and by energy analysis using time of flight mass spectroscopy. The mechanism based on Eqs. (29-31) would have a second order dependence on Ne^+ and H^+ which is kinetically unfavorable. The mechanism based on Eqs. (32-34) requires Ne_2^* which is typically produced at a high rate with high pressure and extremely high microhollow-discharge power densities [57] unlike the conditions in our experiments. Thus, with the current data, the catalysis reaction given by Eqs. (35-37) is the favored mechanism supported by the previous observation of an absence of line broadening with an elevated electron temperature [13]. Characteristics of the power reaction further support this reaction mechanism. The excess power increased disproportionately with the input power as shown in Table 3. This was probably due to the effect of an increase in Ne^+. It is expected that the catalysis reaction given by Eqs. (35-37) would increase the electron density due to the ionization of Ne^+. And, the current was significantly higher in the case of

neon-hydrogen plasmas. The ionization energy of *Ne* is 21.56 eV; whereas, that of *Xe* is 12.13 eV [56]. Yet, for 350 W input power to the neon-hydrogen glow discharge plasma, the current shown in Table 3 was 1.346 A. Whereas, that of the xenon-hydrogen plasma shown in Table 2 was only 1.016 A. Langmuir probe measurements of the electron density and temperature are in progress to confirm this observation.

Additionally, we are investigating the possibility of using the catalytic reaction of atomic hydrogen as a power source for many applications such as a source to internally pump a cw helium-neon laser wherein at least one of neon or helium serves as the catalyst. General power generation is also being pursued.

IV. Conclusion

We report that novel emission lines were observed with energies of $q \cdot 13.6\,eV$ where $q = 1,2,3,4,6,7,8,9,11$ or these lines inelastically scattered by helium atoms wherein $21.2\,eV$ was absorbed in the excitation of $He\,(1s^2)$ to $He\,(1s^1 2p^1)$. These lines were identified as transitions to fractional Rydberg states of atomic hydrogen.

Two $H(1/p)$ atoms may react to form $H_2(1/p)$ that has a bond energy and vibrational levels that are p^2 times those of H_2 comprising uncatalyzed atomic hydrogen where p is an integer. Since the $\upsilon = 0$ to $\upsilon = 1$ vibrational transition of H_2 is a resonant state of the corresponding transition of $H_2(1/2)$, emission due to the reaction $2H(1/2) \rightarrow H_2(1/2)$ is possible with vibronic coupling at $E_{D+vib} = p^2 E_{D\,H_2} \pm \left(\frac{\upsilon^*}{3}\right) E_{vib\,H_2(\upsilon=0\rightarrow\upsilon=1)}$, $\upsilon^* = 1,2,3\ldots$ where $E_{D\,H_2}$ and $E_{vib\,H_2(\upsilon=0\rightarrow\upsilon=1)}$ are the experimental bond and vibrational energies of H_2, respectively. These lines were observed at the predicted energies of $E_{D+vib} = 17.913 \pm \left(\frac{\upsilon^*}{3}\right) 0.515902\,eV$ that matched to longer wavelengths for $\upsilon^* = 2$ to $\upsilon^* = 32$ and to shorter wavelengths for $\upsilon^* = 1$ to $\upsilon^* = 16$ to within the spectrometer resolution of about $\pm 0.05\%$.

Excess power up to $306 \pm 5\,W$ by the catalytic reaction of neon catalyst with atomic hydrogen corresponded to a volumetric power density of $6.8\,MW/m^3$. The excess power increased with power applied to drive the plasma, and the data favors Ne^+ to Ne^{2+} as the catalytic reaction.

The observed power may have many applications such as internally pumping a helium-neon laser. The power density is comparable to that of many natural-gas-fired gas turbines used in electric power generation; thus, electric power generation applications are attractive, especially given that presently observed and previously reported energy balances were over $1000\ eV/H\ atom$ [7, 11, 15-17, 19, 20, 25, 27, 47-49] compared to the energy of combustion of $1.48\ eV/H\ atom$. Since the power is in the form of a plasma, direct high-efficiency, low cost energy conversion may be possible, thus, avoiding a heat engine such as a turbine [10, 24, 32] or a reformer-fuel cell system. A plasmadynamic power converter is already operational in our laboratory [60-61].

Acknowledgment

Special thanks to Ying Lu and Takeyoshi Onuma for recording some spectra.

References

1. N. V. Sidgwick, *The Chemical Elements and Their Compounds*, Volume I, Oxford, Clarendon Press, (1950), p.17.
2. M. D. Lamb, *Luminescence Spectroscopy*, Academic Press, London, (1978), p. 68.
3. H. Conrads, R. Mills, Th. Wrubel, Plasma Sources Science and Technology, submitted.
4. R. L. Mills, P. Ray, Chem. Phys. Letts., submitted.
5. R. L. Mills, B. Dhandapani, J. He, J of Materials Research, submitted.
6. R. L. Mills, A. Voigt, B. Dhandapani, J. He, Int. J. Hydrogen Energy, submitted.
7. R. L. Mills, P. Ray, New Journal of Physics, www.njp.org, Vol. 4, (2002), pp. 22.1-22.17.
8. R. L. Mills, P. Ray, Int. J. Hydrogen Energy, in press.
9. R. L. Mills, E. Dayalan, Proceedings of the 17th Annual Battery Conference on Applications and Advances, California State University, Long Beach, CA, (January 15-18, 2002), pp. 1-6.
10. R. Mayo, R. Mills, M. Nansteel, IEEE Transactions on Plasma Science, in press.

11. R. Mills, P. Ray, J. Dong, M. Nansteel, W. Good, P. Jansson, B. Dhandapani, J. He, Industrial Engineering and Chemical Research, submitted.
12. R. Mills, E. Dayalan, P. Ray, B. Dhandapani, J. He, Electrochimica Acta, in press.
13. R. L. Mills, P. Ray, B. Dhandapani, J. He, J. of Applied Physics, submitted.
14. R. L. Mills, P. Ray, B. Dhandapani, J. He, J. of Phys. Chem. (letter), submitted.
15. R. L. Mills, P. Ray, B. Dhandapani, M. Nansteel, X. Chen, J. He, Chem. Phys. Letts., in press.
16. R. L. Mills, P. Ray, B. Dhandapani, M. Nansteel, X. Chen, J. He, Quantitative Spectroscopy and Energy Transfer, in press.
17. R. L. Mills, P. Ray, B. Dhandapani, M. Nansteel, X. Chen, J. He, J Mol. Struct., in press.
18. R. L. Mills, P. Ray, Int. J. Hydrogen Energy, Vol. 27, No. 9, (2002), pp. 927-935.
19. R. Mills, J. Dong, W. Good, P. Ray, J. He, B. Dhandapani, Int. J. Hydrogen Energy, Vol. 27, No. 9, (2002), pp. 967-978.
20. R. L. Mills, A. Voigt, P. Ray, M. Nansteel, B. Dhandapani, Int. J. Hydrogen Energy, Vol. 27, No. 6, (2002), pp. 671-685.
21. R. Mills, P. Ray, Int. J. Hydrogen Energy, Vol. 27, No. 5, (2002), pp. 533-564.
22. R. Mills, P. Ray, Int. J. Hydrogen Energy, Vol. 27, No. 3, pp. 301-322.
23. R. Mills, P. Ray, Int. J. Hydrogen Energy, Vol. 27, No. 2, (2002), pp. 183-192.
24. R. Mills, Proceedings of the National Hydrogen Association, 12 th Annual U.S. Hydrogen Meeting and Exposition, *Hydrogen: The Common Thread*, The Washington Hilton and Towers, Washington DC, (March 6-8, 2001), pp. 671-697.
25. R. Mills, W. Good, A. Voigt, Jinquan Dong, Int. J. Hydrogen Energy, Vol. 26, No. 11, (2001), pp. 1199-1208.
26. R. Mills, Int. J. Hydrogen Energy, Vol. 26, No. 10, (2001), pp. 1041-1058.
27. R. Mills, N. Greenig, S. Hicks, Int. J. Hydrogen Energy, Vol. 27, No. 6, (2002), pp. 651-670.

28. R. Mills, Global Foundation, Inc. Orbis Scientiae entitled *The Role of Attractive and Repulsive Gravitational Forces in Cosmic Acceleration of Particles The Origin of the Cosmic Gamma Ray Bursts*, (29th Conference on High Energy Physics and Cosmology Since 1964) Dr. Behram N. Kursunoglu, Chairman, December 14-17, 2000, Lago Mar Resort, Fort Lauderdale, FL, Kluwer Academic/Plenum Publishers, New York, pp. 243-258.
29. R. Mills, Int. J. Hydrogen Energy, Vol. 27, No. 5, (2002), pp. 565-590.
30. R. Mills and M. Nansteel, P. Ray, IEEE Transactions on Plasma Science, in press.
31. R. Mills, B. Dhandapani, M. Nansteel, J. He, A. "Voigt, Int. J. Hydrogen Energy, Vol. 26, No. 9, (2001), pp. 965-979.
32. R. Mills, Global Foundation International Conference on "Global Warming and Energy Policy", Dr. Behram N. Kursunoglu, Chairman, Fort Lauderdale, FL, November 26-28, 2000, Kluwer Academic/Plenum Publishers, New York, pp. 1059-1096.
33. R. Mills, Int. J. Hydrogen Energy, Vol. 26, No. 10, (2001), pp. 1059-1096.
34. R. Mills, M. Nansteel, and Y. Lu, J. of Plasma Physics, submitted.
35. R. Mills, J. Dong, Y. Lu, Int. J. Hydrogen Energy, Vol. 25, (2000), pp. 919-943.
36. R. Mills, Int. J. Hydrogen Energy, Vol. 26, No. 6, (2001), pp. 579-592.
37. R. Mills, Int. J. Hydrogen Energy, Vol. 26, No. 4, (2001), pp. 327-332.
38. R. Mills, T. Onuma, and Y. Lu, Int. J. Hydrogen Energy, Vol. 26, No. 7, July, (2001), pp. 749-762.
39. R. Mills, M. Nansteel, and Y. Lu, Int. J. Hydrogen Energy, Vol. 26, No. 4, (2001), pp. 309-326.
40. R. Mills, *The Grand Unified Theory of Classical Quantum Mechanics*, September 2001 Edition, BlackLight Power, Inc., Cranbury, New Jersey, Distributed by Amazon.com.
41. R. Mills, B. Dhandapani, N. Greenig, J. He, Int. J. of Hydrogen Energy, Vol. 25, Issue 12, December, (2000), pp. 1185-1203.
42. R. Mills, Int. J. of Hydrogen Energy, Vol. 25, (2000), pp. 669-683.
43. R. Mills, B. Dhandapani, M. Nansteel, J. He, T. Shannon, A. Echezuria, Int. J. of Hydrogen Energy, Vol. 26, No. 4, (2001), pp. 339-367.
44. R. Mills, Journal of New Materials for Electrochemical Systems, in

press.
45. R. Mills, Fusion Technology, Vol. 37, No. 2, March, (2000), pp. 157-182.
46. R. Mills, Int. J. of Hydrogen Energy, Vol. 25, Issue 12, December, (2000), pp. 1171-1183.
47. Mills, R., Good, W., Fusion Technology, Vol. 28, No. 4, November, (1995), pp. 1697-1719.
48. Mills, R., Good, W., Shaubach, R., Fusion Technology, Vol. 25, 103 (1994).
49. R. Mills and S. Kneizys, Fusion Technol. Vol. 20, 65 (1991).
50. H. Beutler, Z. Physical Chem., Vol. 27B, (1934), pp. 287-302.
51. G. Herzberg, L. L. Howe, Can. J. Phys., Vol. 37, (1959), pp. 636-659.
52. P. W. Atkins, *Physical Chemistry*, Second Edition, W. H. Freeman, San Francisco, (1982), p. 589.
53. NIST Atomic Spectra Database, www.physics.nist.gov/cgi-bin/AtData/display.ksh.
54. J. Y. Roncin, F. Launay, M. Larzilliere, Can. J. Phys., Vol. 62, (1984), pp. 1686-1705.
55. R. Kelly, Journal of Physical and Chemical Reference Data. Part I (H-Cr), Volume 16, (1987), Supplement No. 1, Published by the American Chemical Society and the American Institute of Physics for the National Bureau of Standards, pp. 140-145.
56. D. R. Linde, *CRC Handbook of Chemistry and Physics*, 79 th Edition, CRC Press, Boca Raton, Florida, (1998-9), p. 10-175 to p. 10-177.
57. P. Kurunczi, H. Shah, and K. Becker, J. Phys. B: At. Mol. Opt. Phys., Vol. 32, (1999), L651-L658.
58. S. B. Radovanov, K. Dzierzega, J. R. Roberts, J. K. Olthoff, Appl. Phys. Lett., Vol. 66, No. 20, (1995), pp. 2637-2639.
59. C. Chen, T. Wei, L. R. Collins, and J. Phillips, J. Phys. D: Appl. Phys., Vol. 32, (1999), pp. 688-698.
60. R. Mayo, R. Mills, M. Nansteel, IEEE Transactions on Plasma Science, in press.
61 R. Mayo, R. Mills, "40th Annual Power Sources Conference, Cherry Hill, NJ, June 10-13, (2002), in press.

Table 1. Calculated energies of red and violet series of lines due to the reaction $2H(1/2) \rightarrow H_2(1/2)$ with vibronic coupling and the observed emission lines.

Vibronic Coupling Quantum Number υ *	Calculated [a] Emission (nm)	Calculated [b] Emission (eV)	Observed Lines (nm)	Observed Lines (eV)	Obs. - Cal. (eV)
32	99.905	12.410	99.90	12.41	0.001
31	98.540	12.582	98.50	12.59	0.005
30	97.211	12.754	97.20	12.76	0.001
29	95.918	12.926	95.90	12.93	0.002
28	94.659	13.098	94.70	13.09	-0.006
27	93.432	13.270	93.45	13.27	-0.003
26	92.237	13.442	92.25	13.44	-0.002
25	91.072	13.614	91.05	13.62	0.003
24	89.936	13.786	89.93	13.79	0.001
23	88.828	13.958	88.80	13.96	0.004
22	87.746	14.130	87.75	14.13	-0.001
21	86.691	14.302	86.70	14.30	-0.001
20	85.661	14.474	85.65	14.48	0.002
19	84.656	14.646	84.65	14.65	0.001
18	83.673	14.818	83.60	14.83	0.013
17	82.713	14.990	82.70	14.99	0.002
16	81.775	15.162	81.75	15.17	0.005
15	80.858	15.334	80.90	15.33	-0.008
14	79.961	15.506	79.95	15.51	0.002
13	79.084	15.678	79.10	15.67	-0.003
12	78.226	15.850	78.20	15.85	0.005
11	77.386	16.022	77.40	16.02	-0.003
10	76.565	16.194	76.60	16.19	-0.007
9	75.760	16.366	75.75	16.37	0.002
8	74.972	16.537	74.95	16.54	0.005
7	74.201	16.709	74.20	16.71	0.000
6	73.445	16.881	73.45	16.88	-0.001
5	72.704	17.053	72.70	17.05	0.001
4	71.978	17.225	71.95	17.23	0.007
3	71.267	17.397	71.30	17.39	-0.008
2	70.569	17.569	70.60	17.56	-0.008
1	68.556	18.085	68.60	18.07	-0.012
2	67.911	18.257	67.90	18.26	0.003
3	67.277	18.429	67.25	18.44	0.007
4	66.655	18.601	66.65	18.60	0.001
5	66.044	18.773	66.05	18.77	-0.002
6	65.445	18.945	65.45	18.94	-0.002
7	64.856	19.117	64.85	19.12	0.002
8	64.278	19.289	64.25	19.30	0.008
9	63.710	19.461	63.70	19.46	0.003
10	63.152	19.633	63.15	19.63	0.001
11	62.604	19.805	62.60	19.81	0.001
12	62.065	19.977	62.05	19.98	0.005
13	61.535	20.149	61.55	20.14	-0.005
14	61.014	20.321	61.00	20.33	0.005
15	60.502	20.493	60.50	20.49	0.001
16	59.999	20.665	60.00	20.66	0.000

[a] Eq. (13) for red series with wavelengths longer than 69.214 nm and Eq. (14) for violet series with wavelengths shorter than 69.214 nm wherein 69.214 nm corresponds to the bond energy of $H_2(1/2)$.

[b] Eqs. (13-14) and Planck's equation $\lambda = \frac{hc}{E}$.

Table 2. Temperature rise variation with power input to the xenon-hydrogen plasma.

Input Power (W)	Voltage (V)	Current (A)	Temp. Rise Above 210.0 °C ΔT (± 0.1 °C)
65.0	314.8	0.207	39.0
100	334.1	0.299	57.0
150	327.8	0.458	72.7
200	365.0	0.548	91.4
250	367.3	0.681	108.4
300	349.6	0.858	126.3
350	344.6	1.016	137.5
400	340.2	1.176	148.8

Table 3. The total output power and excess power at selected input powers for the neon-hydrogen plasma.

Input Power (W)	Voltage (V)	Current (A)	Temp. Rise Above 210.0 °C ΔT ($\pm 0.1\,^{\circ}C$)	Total Output Power Q ($\pm 5\,W$) Eq. (27)	Excess Power Q_{gen} ($\pm 5\,W$) Eq. (28)
100	212.8	0.470	66.7	129.0	29.0
150	227.2	0.660	95.9	208.7	58.7
200	232.5	0.861	124.7	303.3	103.3
250	232.6	1.075	158.2	435.7	185.7
300	262.7	1.142	180.8	539.7	239.7
350	260.1	1.346	203.3	656.2	306.2

Figure Captions

Figure 1. The experimental set up comprising a microwave discharge cell light source and an EUV spectrometer which was differentially pumped.

Figure 2. Cross sectional view of the discharge cell.

Figure 3. The experimental set up comprising a discharge gas cell light source and an EUV spectrometer which was differentially pumped.

Figure 4. Cylindrical stainless steel glow discharge cell and the compound hollow cathode used for power balance studies.

Figure 5. The experimental setup for generating a glow discharge plasma and for measuring the power balance.

Figure 6. The EUV spectra ($17.5-50\,nm$) of the microwave cell emission of the helium-hydrogen (98/2%) mixture (top curve) recorded at 20 Torr with a normal incidence EUV spectrometer and a CEM, and control helium (bottom curve) recorded at 20 Torr with a 4° grazing incidence EUV spectrometer and a CEM. Only known He I and He II peaks were observed with the helium control. Reproducible novel emission lines were observed at $45.6\,nm$ and $30.4\,nm$ with energies of $q \cdot 13.6\,eV$ where $q = 2\ or\ 3$ (Eqs. (2a, 2c)) and at $37.4\,nm$ and $20.5\,nm$ with energies of $q \cdot 13.6\,eV$ where $q = 4\ or\ 6$ that were inelastically scattered by helium atoms wherein $21.2\,eV$ was absorbed in the excitation of $He\,(1s^2)$ to $He\,(1s^1 2p^1)$ as proposed in Eq. (23).

Figure 7. The short wavelength EUV spectra ($5-65\,nm$) of the microwave cell emission of the helium-hydrogen (98/2%) mixture (top curve) and control hydrogen (bottom curve) recorded at 1 Torr with a normal incidence EUV spectrometer and a CEM. No hydrogen emission was observed in this region, and no instrument artifacts were observed. Reproducible novel emission lines were observed at $45.6\,nm$, $30.4\,nm$, $13.03\,nm$, $10.13\,nm$, and $8.29\,nm$ with energies of $q \cdot 13.6\,eV$ where $q = 2,3,7,9,\ or\ 11$ and at $37.4\,nm$, $20.5\,nm$, and $14.15\,nm$ with energies of $q \cdot 13.6\,eV$ where $q = 4,6,\ or\ 8$ that were inelastically scattered by helium atoms wherein $21.2\,eV$ was absorbed in the excitation of $He\,(1s^2)$ to $He\,(1s^1 2p^1)$ as proposed in Eq. (23).

Figure 8. The EUV spectrum (20-125 nm) of the control hydrogen discharge cell emission that was recorded with a normal incidence EUV

spectrometer and a CEM. No emission was observed below 80 nm.

Figure 9. The EUV spectra (20-50 nm) of the control xenon (top curve), control xenon-hydrogen (98/2%) mixture (middle curve), and control hydrogen (bottom curve) glow discharge cell emission that was recorded with a 4° grazing incidence EUV spectrometer and a CEM. No peaks were observed in this region from any of the controls. No instrument artifacts were observed.

Figure 10. The EUV spectra (40-100 nm) of the control xenon (top curve), control xenon-hydrogen (98/2%) mixture (middle curve), and control hydrogen (bottom curve) glow discharge cell emission that was recorded with a normal incidence EUV spectrometer and a CEM. No peaks were observed in this region from xenon alone. Only hydrogen peaks were observed at wavelengths greater than about 85 nm with the addition of hydrogen. No instrument artifacts were observed.

Figure 11. The EUV spectrum (20-100 nm) of the control helium microwave discharge cell emission at 1 Torr that was recorded with a normal incidence EUV spectrometer and a CEM. Only known He I and He II peaks were observed.

Figure 12. The EUV spectrum (5-100 nm) of the microwave cell emission of the helium-hydrogen (98/2%) mixture recorded at 1 Torr with a normal incidence EUV spectrometer and a CEM. Reproducible novel emission lines were observed at $45.6\,nm$, $30.4\,nm$, and $8.29\,nm$ with energies of $q \cdot 13.6\,eV$ where $q = 2,3,\, or\, 11$ and at $37.4\,nm$ and $20.5\,nm$ with energies of $q \cdot 13.6\,eV$ where $q = 4\, or\, 6$ that were inelastically scattered by helium atoms wherein $21.2\,eV$ was absorbed in the excitation of $He(1s^2)$ to $He(1s^1 2p^1)$ as proposed in Eq. (23). In addition, a novel series of sharp wavelength-labeled peaks were observed in the 60-100 nm region that were assigned to members of peaks predicted at $E_{D+vib} = 17.913 \pm \left(\frac{\upsilon^*}{3}\right) 0.515902\,eV$ due to the reaction $2H(1/2) \rightarrow H_2(1/2)$ with vibronic coupling. The peaks assigned in Table 1 corresponded to members of the red series $\upsilon^* = 2$ to $\upsilon^* = 32$ and the violet series $\upsilon^* = 1$ to $\upsilon^* = 16$.

Figure 13. The overlaid spectra (60-100 nm) of the microwave cell emission of the helium-hydrogen (98/2%) plasma (top) and the hydrogen plasma (bottom). Hydrogen has no peaks short of 80 nm, and some of the

peaks that are wavelength-labeled and assigned to $H_2(1/2)$ formation in Table 1 do not appear to be due to hydrogen.

Figure 14. The three EUV spectra (48-65 nm) of the glow discharge cell emission of the helium-hydrogen (98/2%) plasma showing peaks of the $E_{D+vib} = 17.913 \pm \left(\frac{\upsilon^*}{3}\right) 0.515902\, eV$ series recorded with a 4° grazing incidence EUV spectrometer and a CEM.

Figure 15. The EUV spectrum (50-65 nm) of the control helium microwave discharge cell emission at 20 Torr that was recorded with a normal incidence EUV spectrometer and a CEM. Only known He I peaks were observed.

Figure 16. Three EUV spectra (60-100 nm) of the microwave cell emission of the helium-hydrogen (98/2%) plasma that showed peaks assigned in Table 1 equivalent to those shown in Figure 14.

Figure 17. Two EUV spectra (45-100 nm) of the microwave cell emission of the helium-hydrogen (98/2%) plasma that showed peaks equivalent to those shown in Figures 14 and 16. The series of peaks due to vibronic coupling is centered about the bond energy of 17.913 eV given by Eq. (12).

Figure 18. Two EUV spectra (45-100 nm) of the microwave cell emission of the helium-hydrogen (98/2%) plasma of Figure 17 shown without the wavelengths of the novel peaks labeled.

Figure 19. The EUV spectrum (62.5-100 nm) of the microwave cell emission of the helium-hydrogen (98/2%) plasma recorded with a normal incidence EUV spectrometer and a CEM showing peaks of the $E_{D+vib} = 17.913 \pm \left(\frac{\upsilon^*}{3}\right) 0.515902\, eV$ series about the position of the $H_2(1/2)$ bond energy corresponding to a wavelength of 69.214 nm. The red series started with $\upsilon^* = 2$, and the violet series started with $\upsilon^* = 1$ corresponding to the peaks at 70.60 nm and 68.60, respectively. The presence of a peak at 67.70 nm which was separated by about 0.06 eV from the predicted $\upsilon^* = 2$ violet series peak at 67.90 nm was assigned to rotational as well as vibronic coupling. Many of the peaks showed rotational features.

Figure 20. The plot of the theoretical emission vacuum wavelengths $E_{D H_2}$ due to the reaction $2H(1/2) \rightarrow H_2(1/2)$ with vibronic coupling at energies of $E_{D+vib} = p^2 E_{D H_2} \pm \left(\frac{\upsilon^*}{3}\right) E_{vib\, H_2(\upsilon=0\rightarrow\upsilon=1)}$ $(p = 2)$ and the

wavelengths observed as shown in Figures 12-14 and 16-19 and given in Table 1. The data matched to longer wavelengths for $\upsilon^* = 2$ to $\upsilon^* = 32$ and to shorter wavelengths for $\upsilon^* = 1$ to $\upsilon^* = 16$ to within the spectrometer resolution of about $\pm 0.05\%$.

Figure 21. The EUV spectrum (20-100 nm) of the control neon microwave discharge cell emission that was recorded with a normal incidence EUV spectrometer and a PMT and a sodium salicylate scintillator. Only known Ne I peaks were observed.

Figure 22. The EUV spectrum (50-100 nm) of the microwave cell emission of the neon-hydrogen (99.5/0.5%) mixture recorded at 300 mTorr with a normal incidence EUV spectrometer and a CEM. A reproducible novel series of wavelength-labeled peaks was observed that was assigned in Table 1 to members of peaks predicted at $E_{D+vib} = 17.913 \pm \left(\frac{\upsilon^*}{3}\right) 0.515902\ eV$ due to the reaction $2H(1/2) \rightarrow H_2(1/2)$ with vibronic coupling.

Figure 23. The EUV spectrum (55-100 nm) of the microwave cell emission from a neon-hydrogen (99.5/0.5%) plasma that showed peaks assigned in Table 1 equivalent to those shown in Figure 22.

Figure 24. The 55-85 nm region of Figure 23.

Figure 25. The EUV spectra (50-100 nm) of the microwave cell emission from a neon-hydrogen (99.5/0.5%) plasma as the pressure was varied from 200 mTorr to 575 mTorr. The novel series of peaks due to the formation of $H_2(1/2)$ showed slight pressure dependence; whereas, continuum peaks to shorter and to longer wavelengths were observed only as the pressure was increased from 200 to 575 mTorr.

Figure 26. The temperature increase above the constant kiln temperature of $210 \pm 0.1\ ^\circ C$ as a function of the power applied to each of the gas mixtures. Significant excess power was observed in the case of neon-hydrogen plasmas; whereas, no excess power was observed from xenon-hydrogen plasmas.

Figure 27. The EUV spectrum (25-55 nm) of the glow discharge cell emission of the neon-hydrogen (99.5/0.5%) mixture recorded with a normal incidence EUV spectrometer and a CEM. Ne^{2+} was observed at 49.1, 37.9, 32.8, 31.3, 30.8, 30.1, 28.4, and 26.7 nm. Ne^{+} was observed at 46.07, 44.7, 40.7, 36.24, 35.7, 35.4, 33.1, and 32.8 nm.

Fig. 1

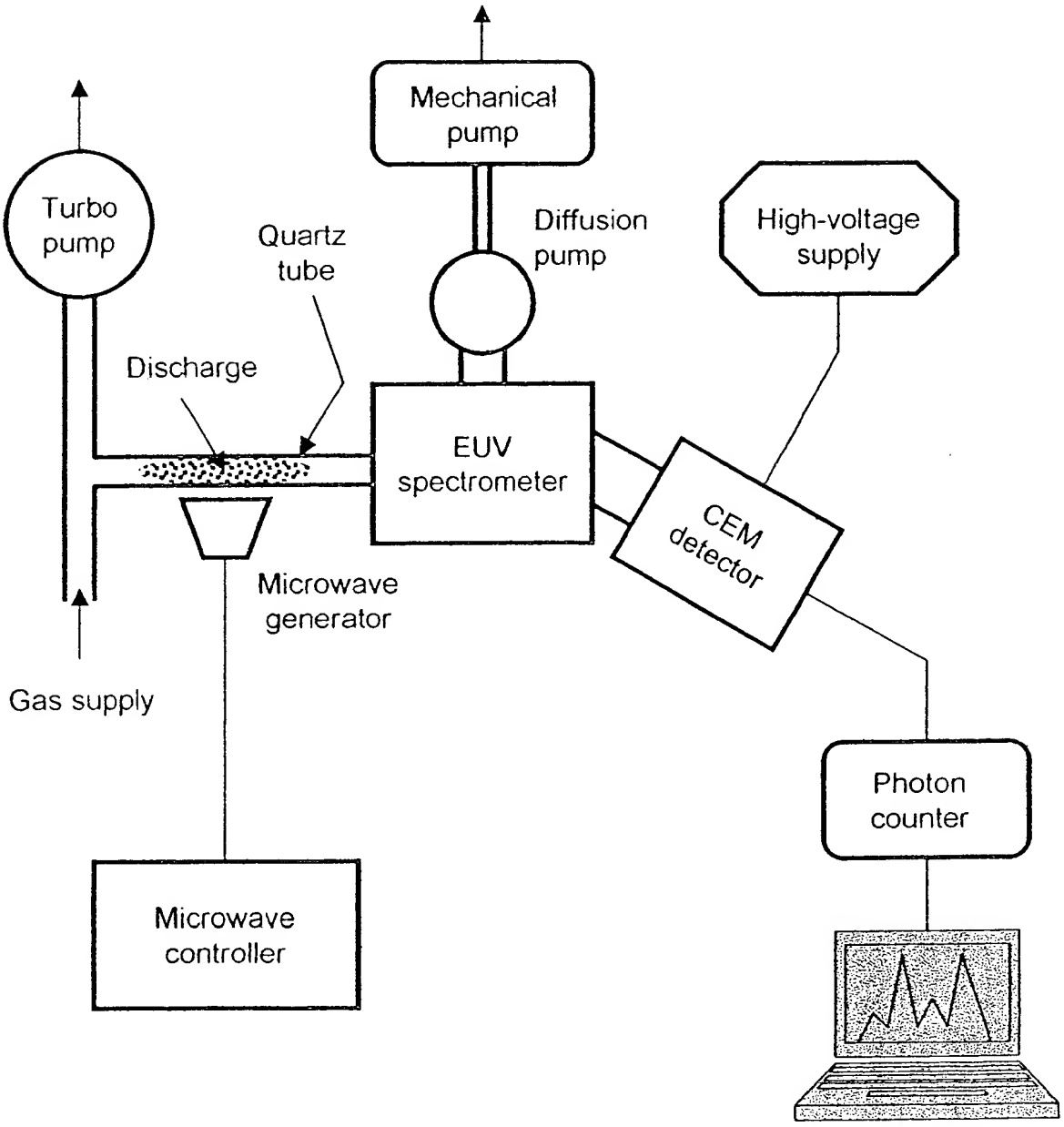
Mechanical pump
Turbo pump
Quartz tube
Diffusion pump
High-voltage supply
Discharge
EUV spectrometer
CEM detector
Microwave generator
Gas supply
Photon counter
Microwave controller

Fig. 2

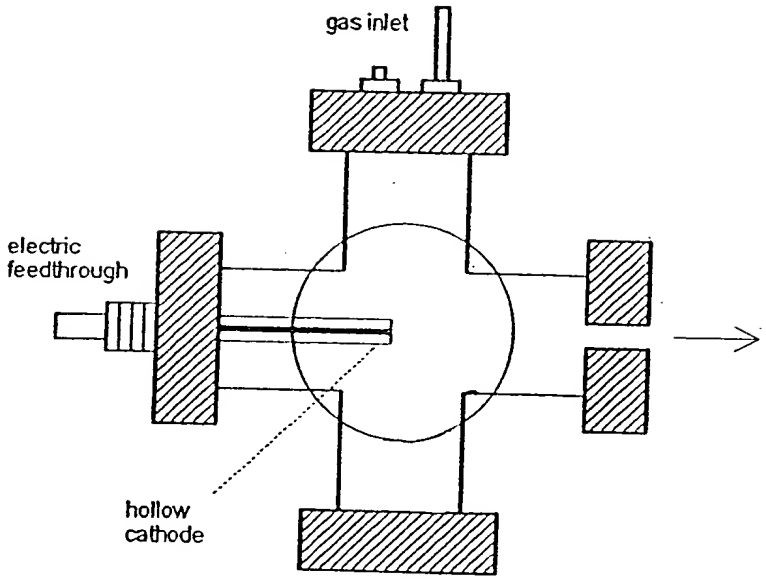

Fig. 3

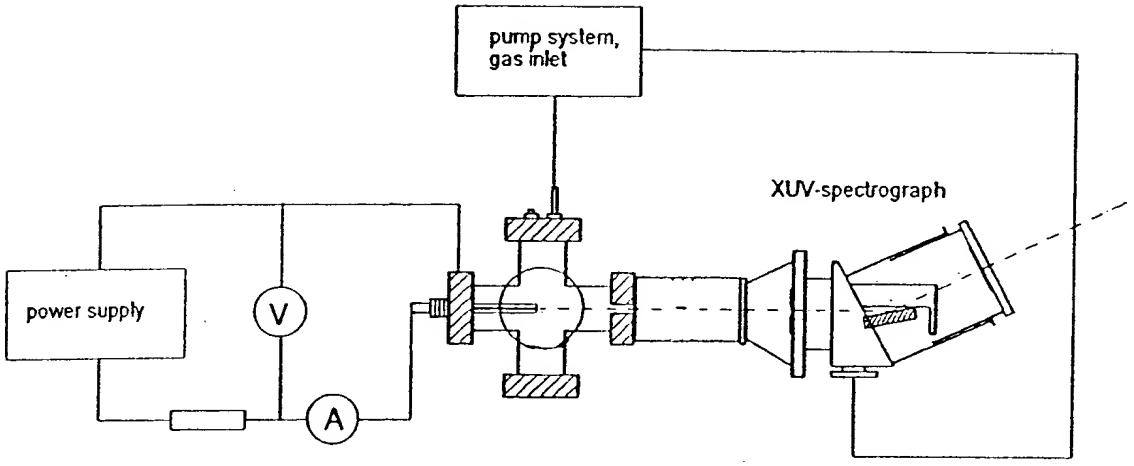

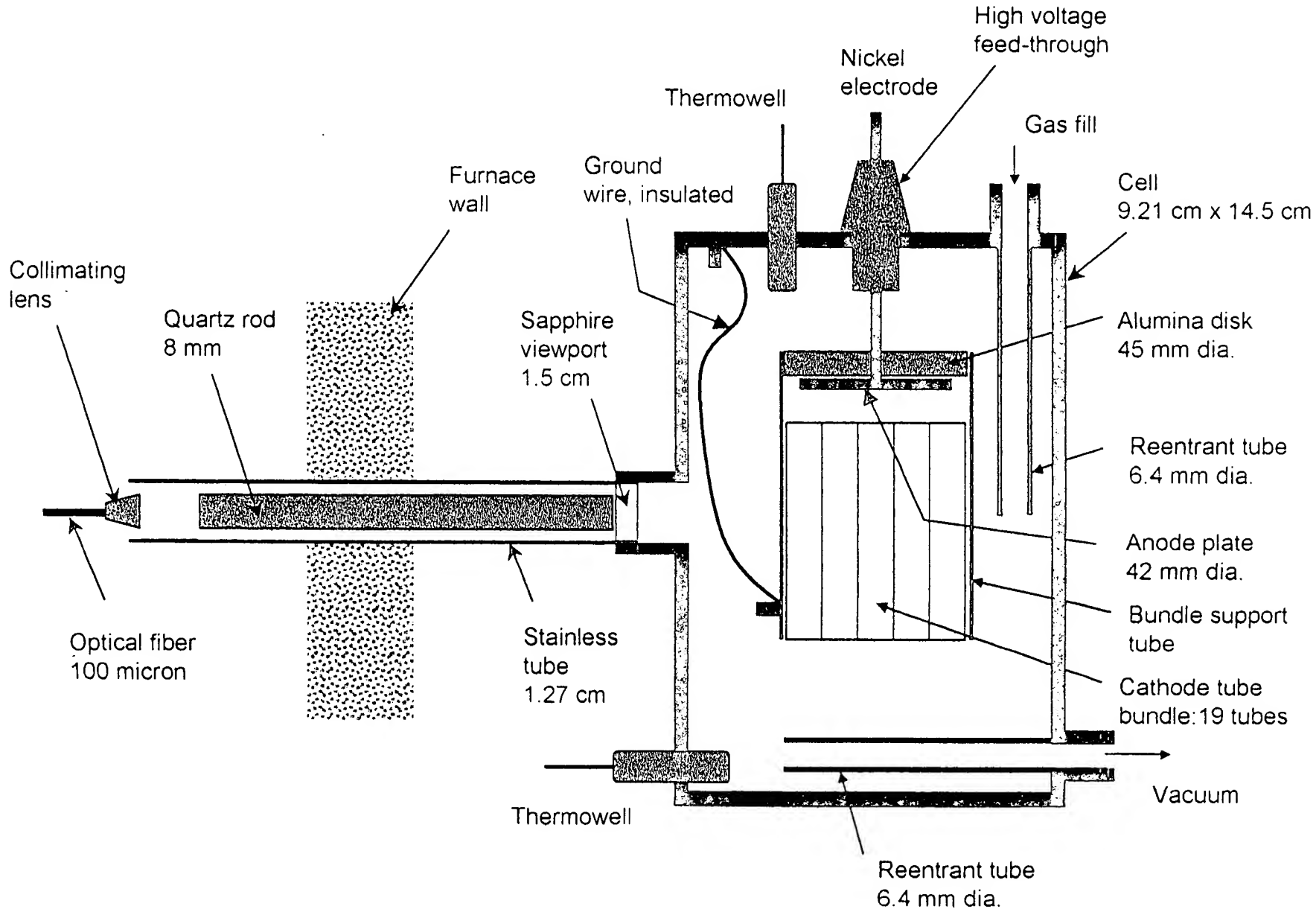
High voltage
feed-through
Nickel
electrode
Thermowell
Gas fill
Furnace
wall
Ground
wire, insulated
Cell
9.21 cm x 14.5 cm
Collimating
lens
Quartz rod
8 mm
Sapphire
viewport
1.5 cm
Alumina disk
45 mm dia.
Reentrant tube
6.4 mm dia.
Anode plate
42 mm dia.
Bundle support
tube
Cathode tube
bundle:19 tubes
Optical fiber
100 micron
Stainless
tube
1.27 cm
Vacuum
Thermowell
Reentrant tube
6.4 mm dia.

Fig. 4

Fig. 5

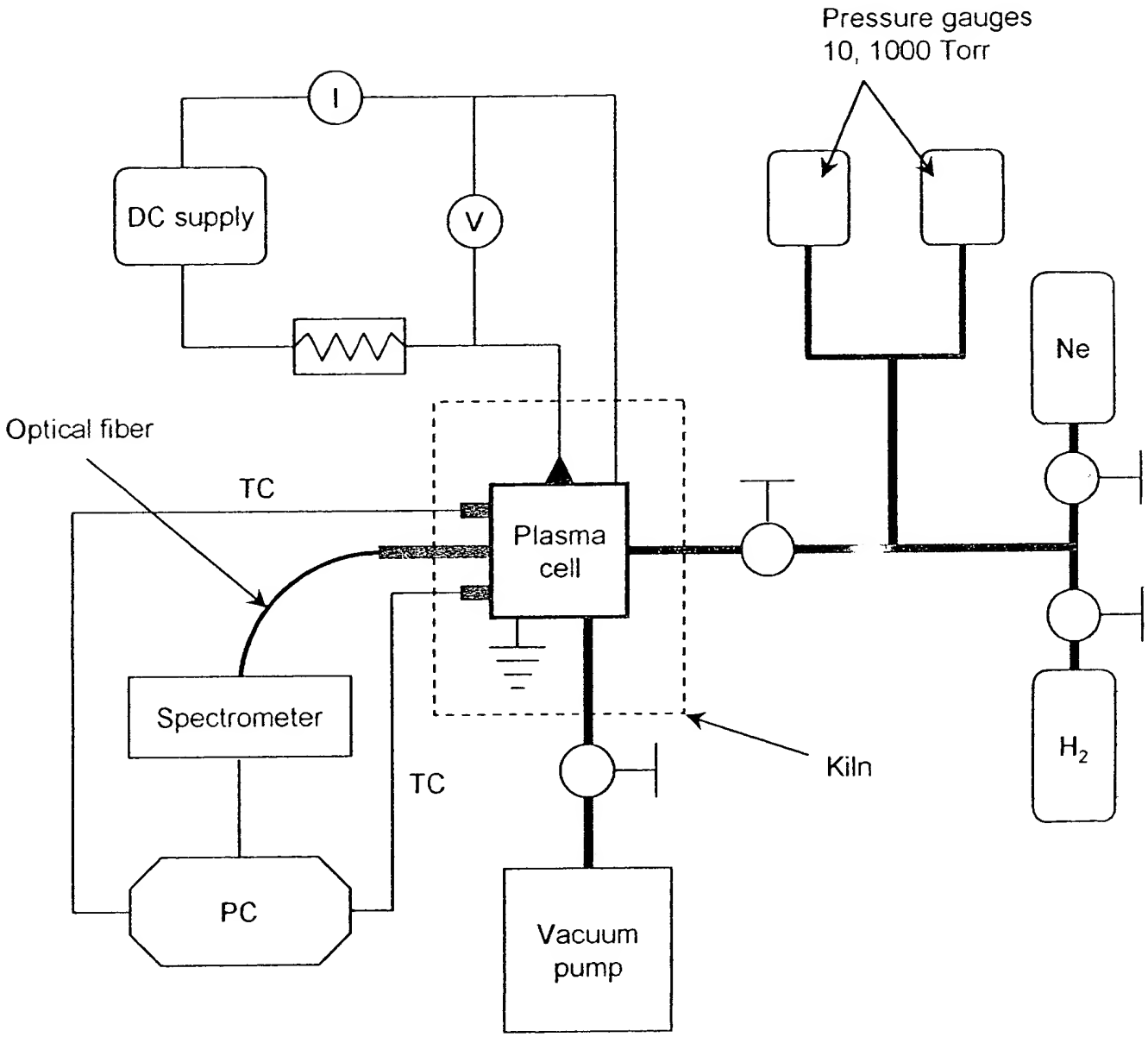
Pressure gauges
10, 1000 Torr
I
DC supply
V
Ne
Optical fiber
TC
Plasma
cell
Spectrometer
TC
Kiln
H_2
PC
Vacuum
pump

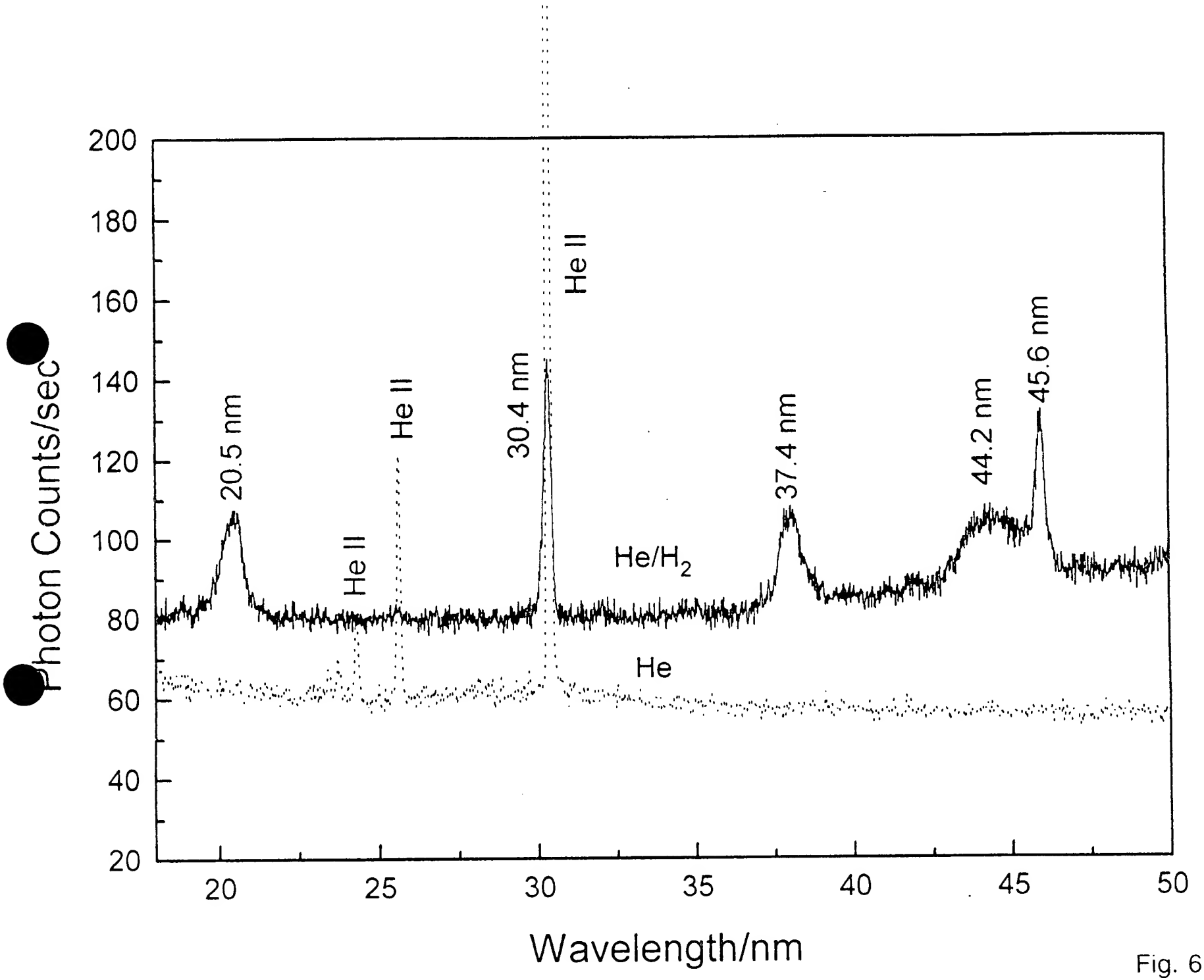
Photon Counts/sec
200
180
160
140
120
100
80
60
40
20
20.5 nm
He II
He II
30.4 nm
He II
He/H2
37.4 nm
44.2 nm
45.6 nm
He
20
25
30
35
40
45
50
Wavelength/nm

Fig. 6

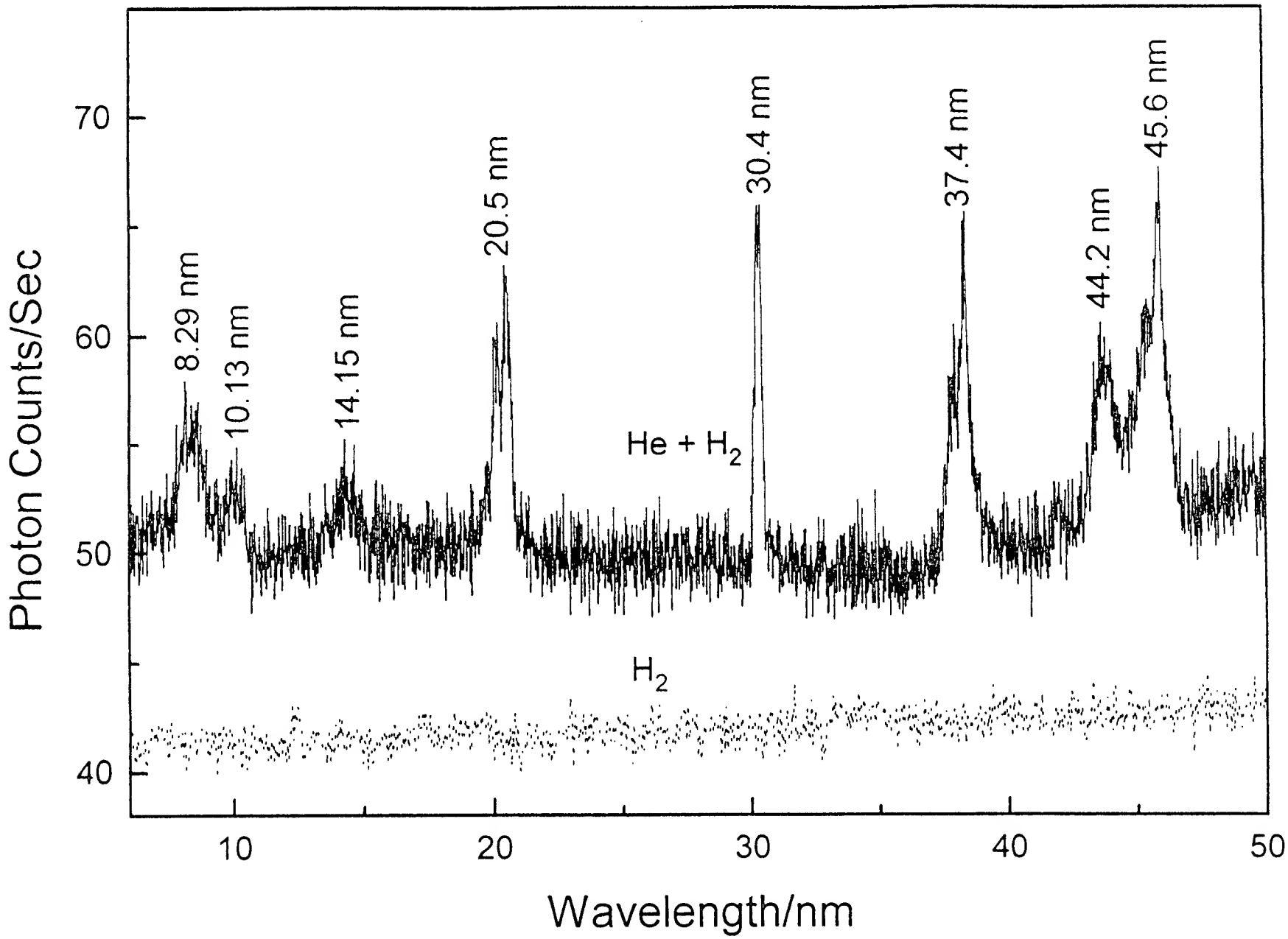
Photon Counts/Sec
70
60
50
40
8.29 nm
10.13 nm
14.15 nm
20.5 nm
30.4 nm
37.4 nm
44.2 nm
45.6 nm
He + H2
H2
10
20
30
40
50
Wavelength/nm

Fig. 7

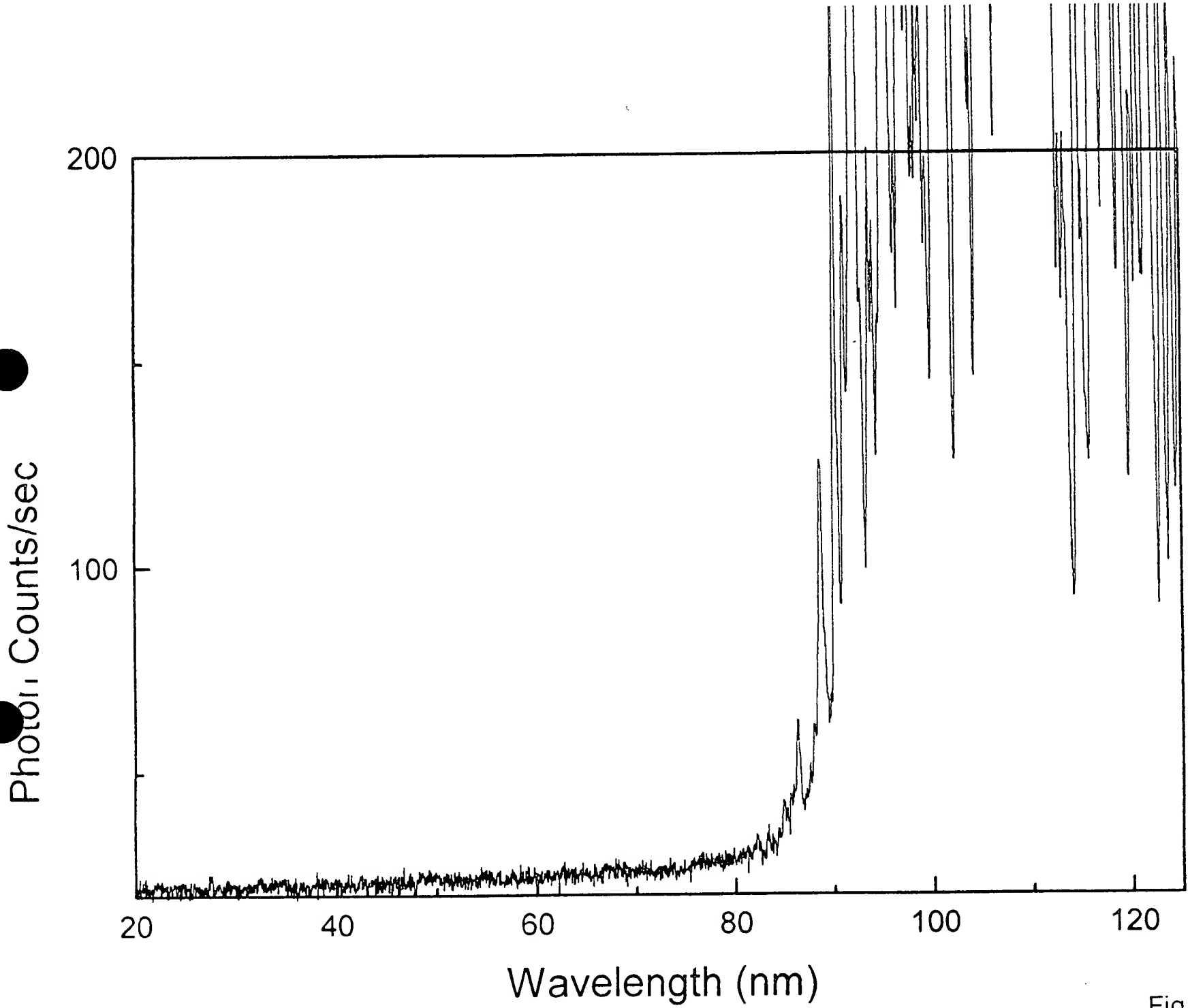

Fig. 8

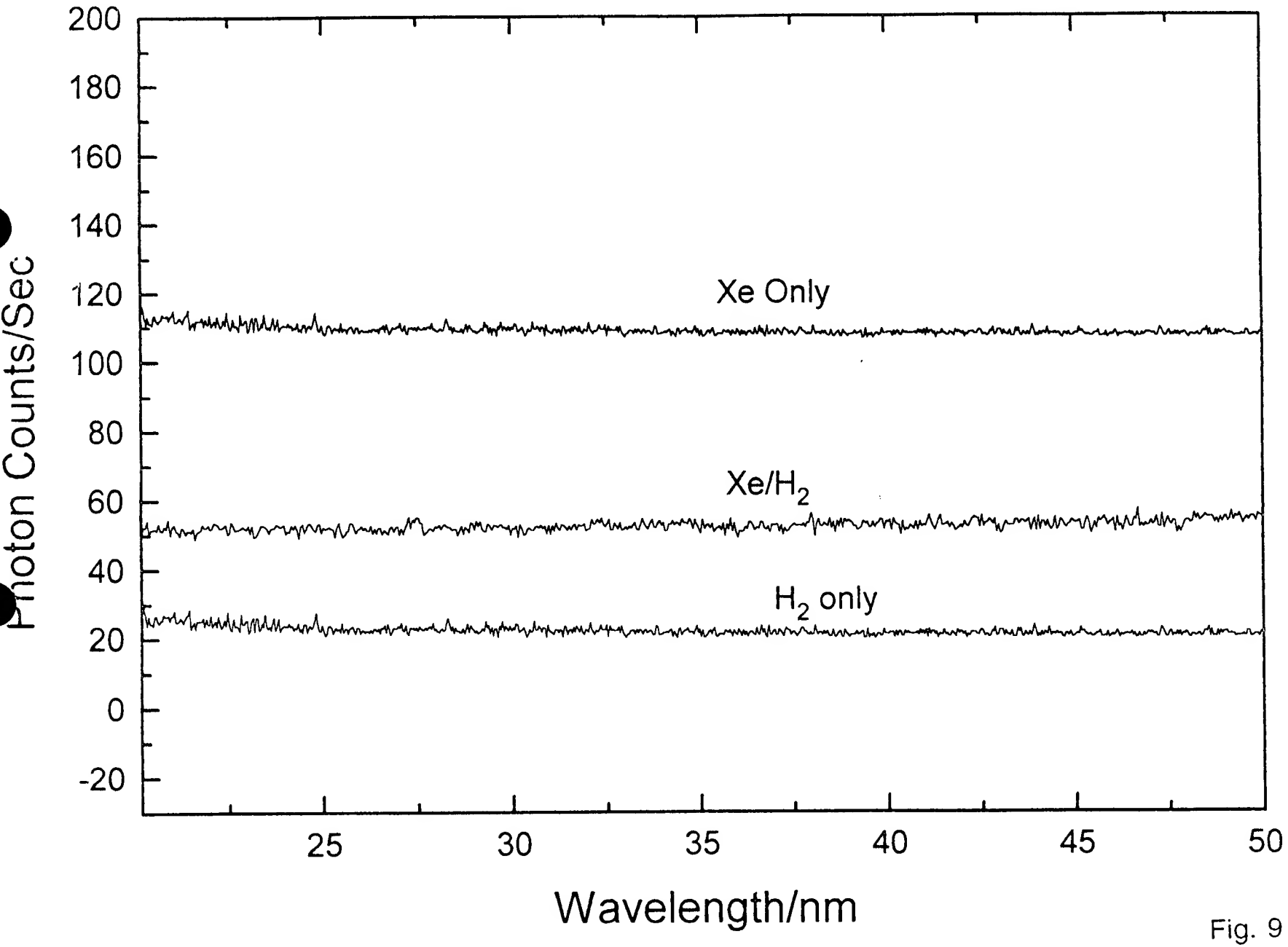
Photon Counts/Sec
200
180
160
140
120
100
80
60
40
20
0
-20
Xe Only
Xe/H2
H2 only
25
30
35
40
45
50
Wavelength/nm

Fig. 9

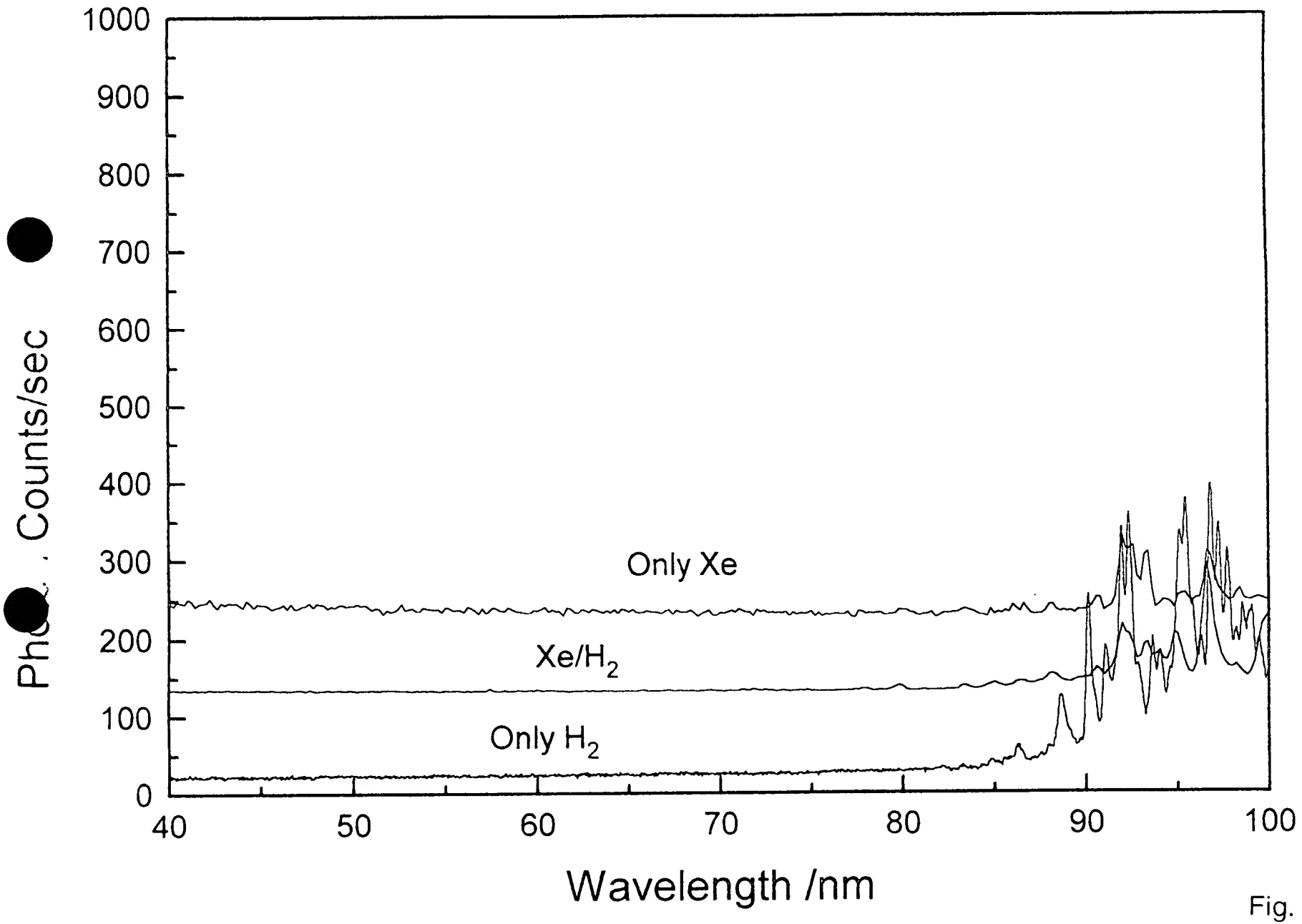
1000
900
800
700
600
500
400
300
200
100
0
Counts/sec
Only Xe
Xe/H2
Only H2
40
50
60
70
80
90
100
Wavelength /nm

Fig. 10

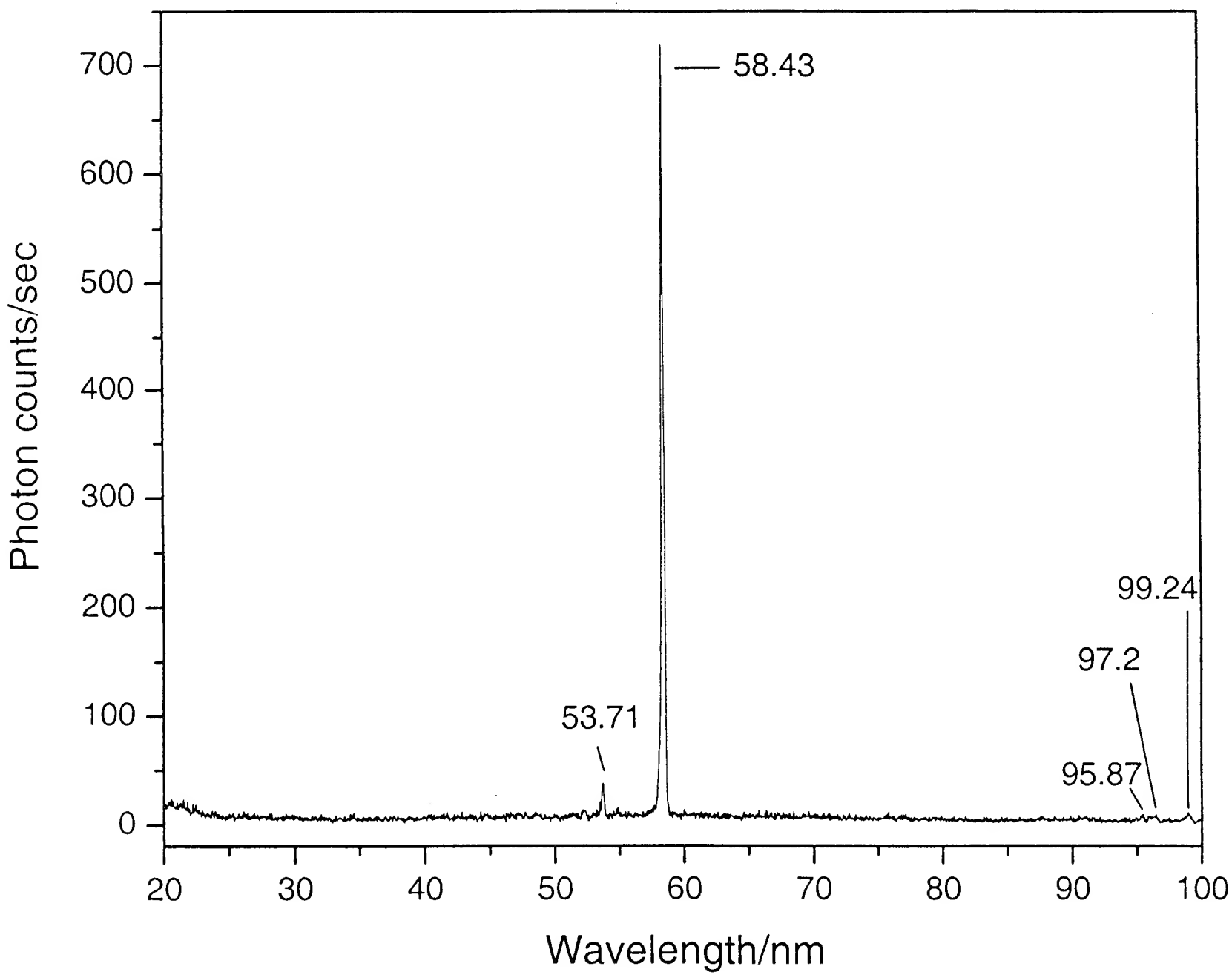
Photon counts/sec
700
600
500
400
300
200
100
0
20
30
40
50
60
70
80
90
100
Wavelength/nm
58.43
53.71
99.24
97.2
95.87

Fig. 11

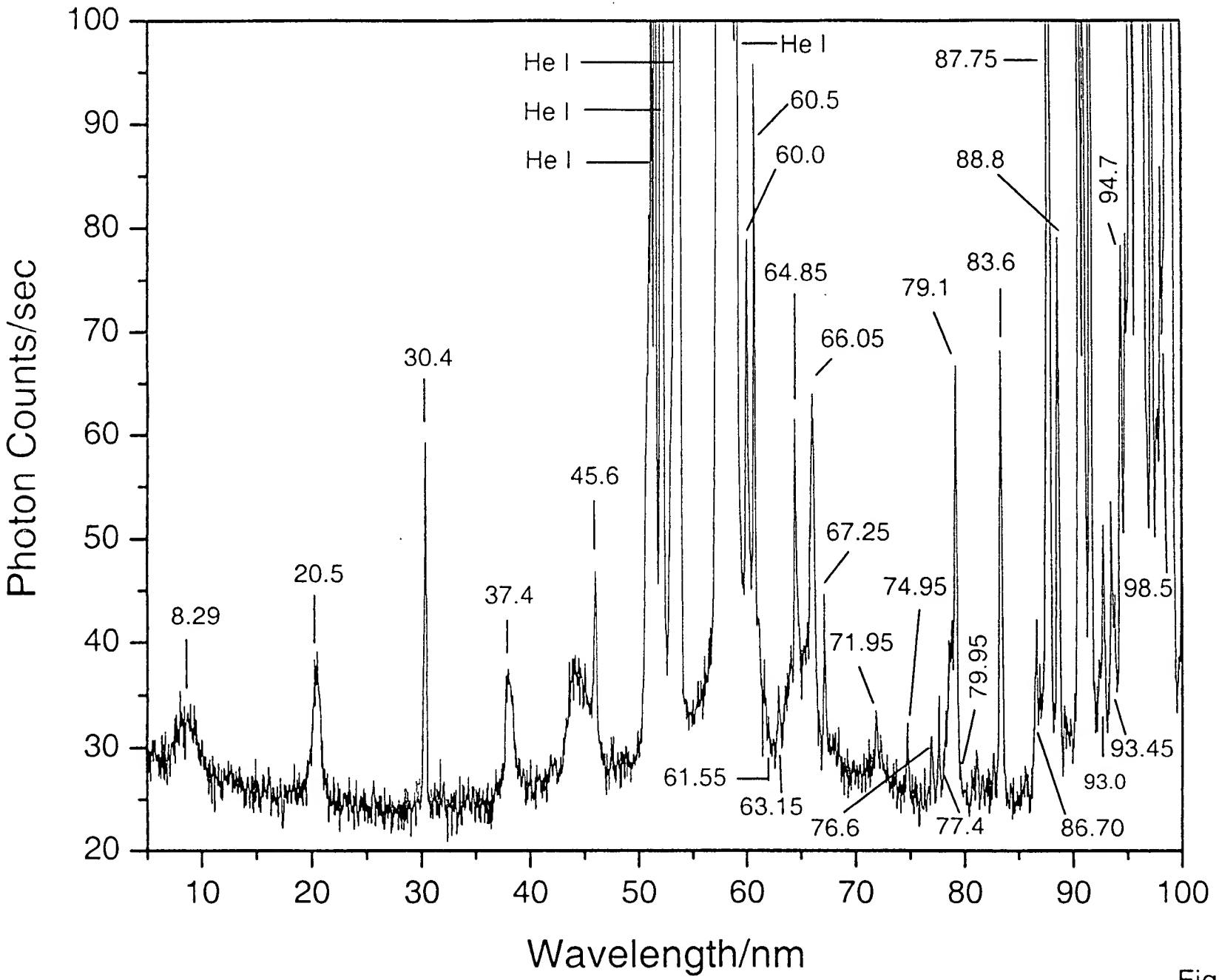
Photon Counts/sec
Wavelength/nm
He I
He I
He I
He I
60.5
60.0
87.75
88.8
94.7
64.85
83.6
79.1
66.05
30.4
45.6
67.25
20.5
37.4
74.95
98.5
71.95
79.95
8.29
93.45
61.55
93.0
63.15
76.6
77.4
86.70

Fig. 12

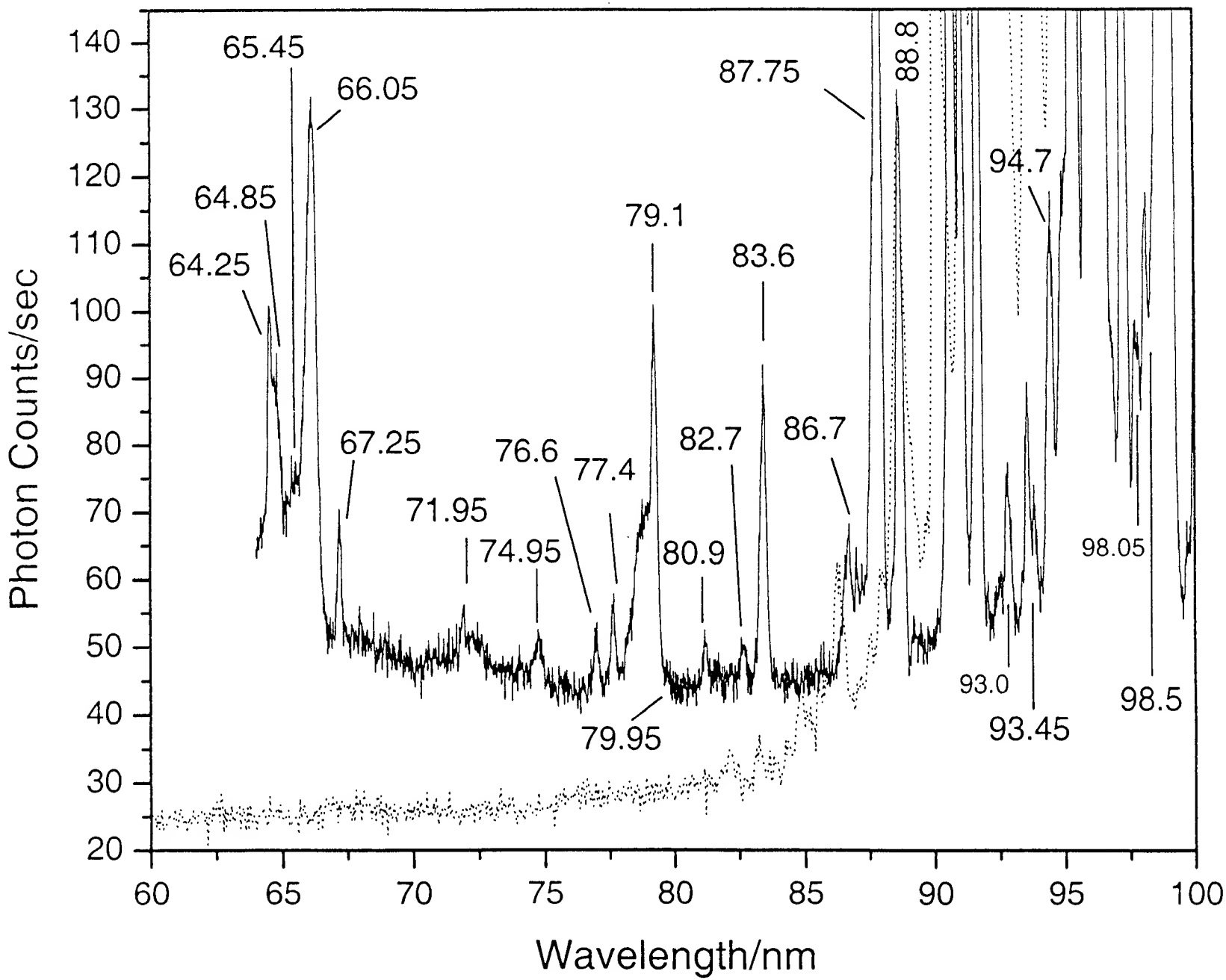
Photon Counts/sec
Wavelength/nm
65.45
66.05
64.85
64.25
67.25
71.95
74.95
76.6
77.4
79.1
79.95
80.9
82.7
83.6
86.7
87.75
88.8
93.0
93.45
94.7
98.05
98.5

Fig. 13

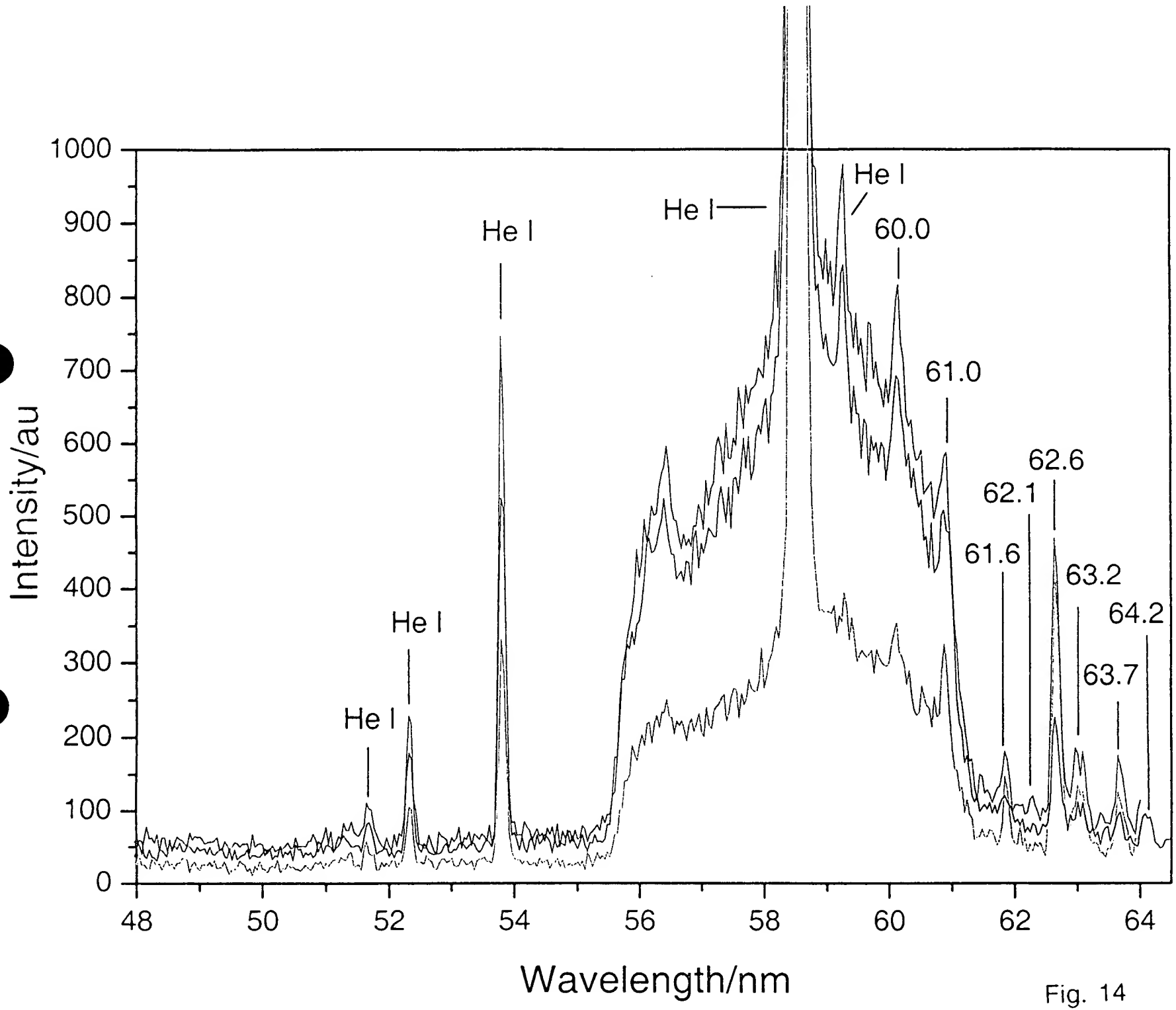
1000
900
800
700
600
500
400
300
200
100
0
Intensity/au
48
50
52
54
56
58
60
62
64
Wavelength/nm
He I
He I
He I
He I
He I
60.0
61.0
61.6
62.1
62.6
63.2
63.7
64.2

Fig. 14

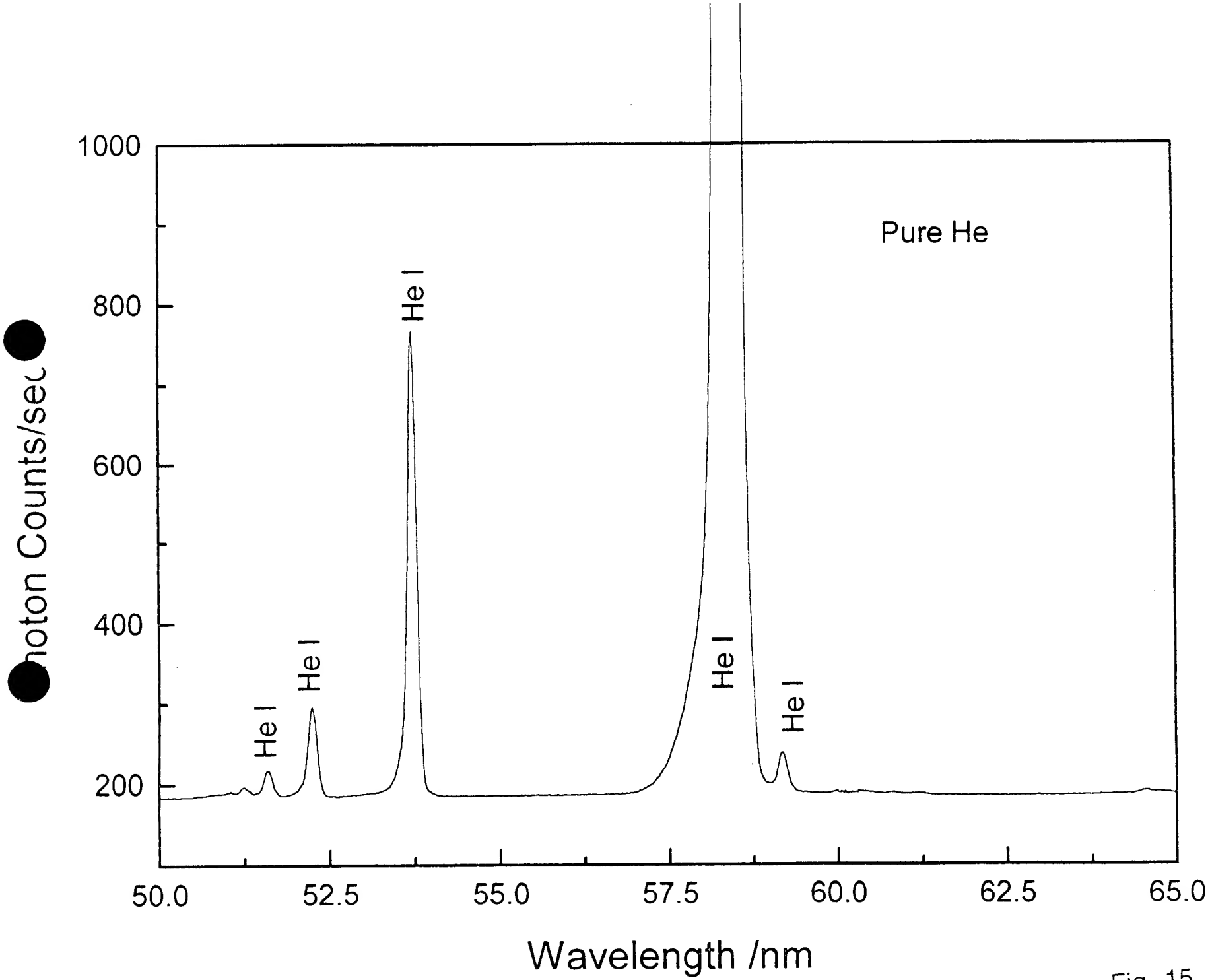
1000
800
600
400
200
Photon Counts/sec
Pure He
He I
He I
He I
He I
He I
50.0
52.5
55.0
57.5
60.0
62.5
65.0
Wavelength /nm

Fig. 15

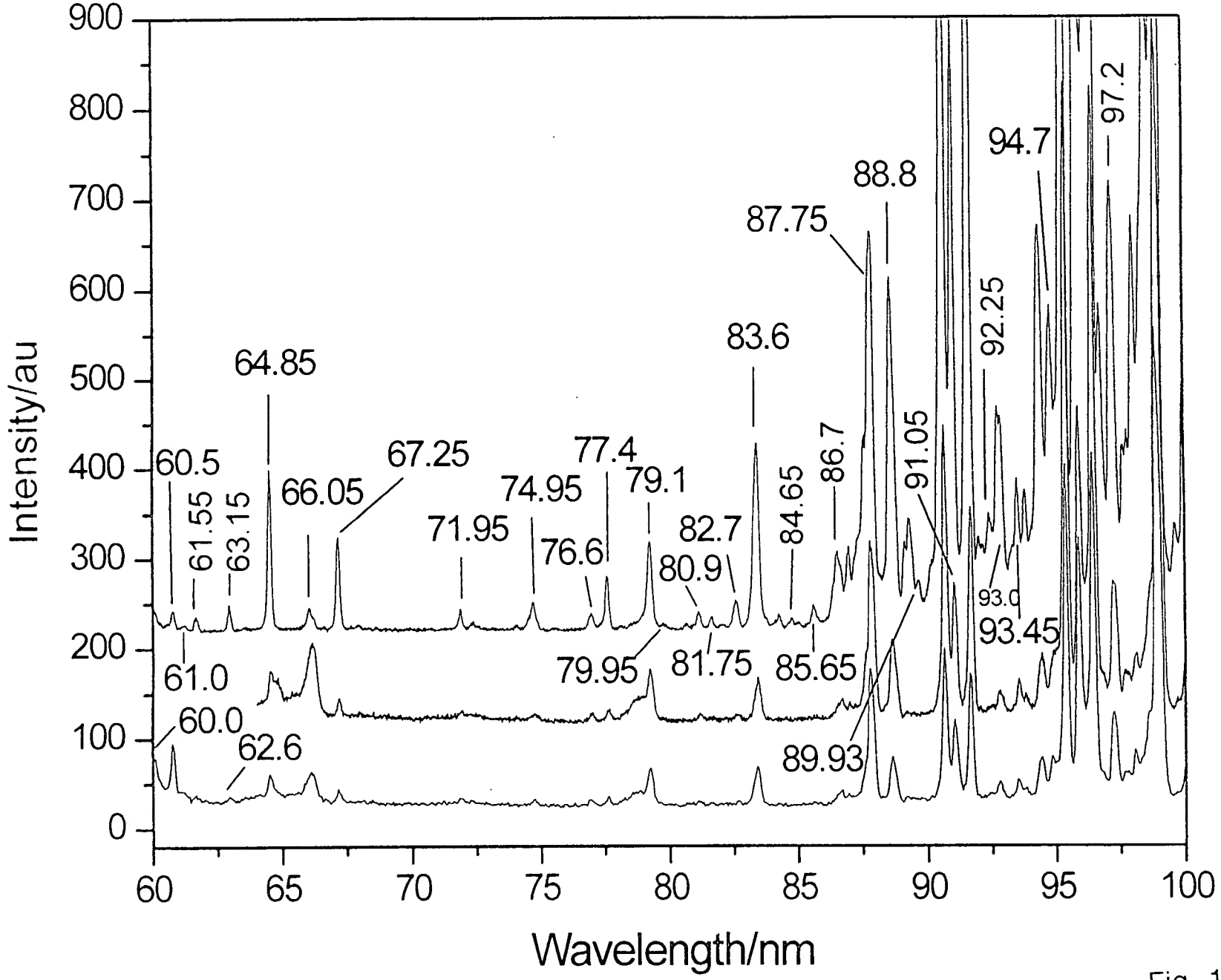
Intensity/au
Wavelength/nm
900
800
700
600
500
400
300
200
100
0
60
65
70
75
80
85
90
95
100
60.5
61.55
63.15
64.85
66.05
67.25
71.95
74.95
76.6
77.4
79.1
80.9
82.7
83.6
84.65
86.7
87.75
88.8
91.05
92.25
93.0
93.45
94.7
97.2
61.0
79.95
81.75
85.65
60.0
62.6
89.93

Fig. 16

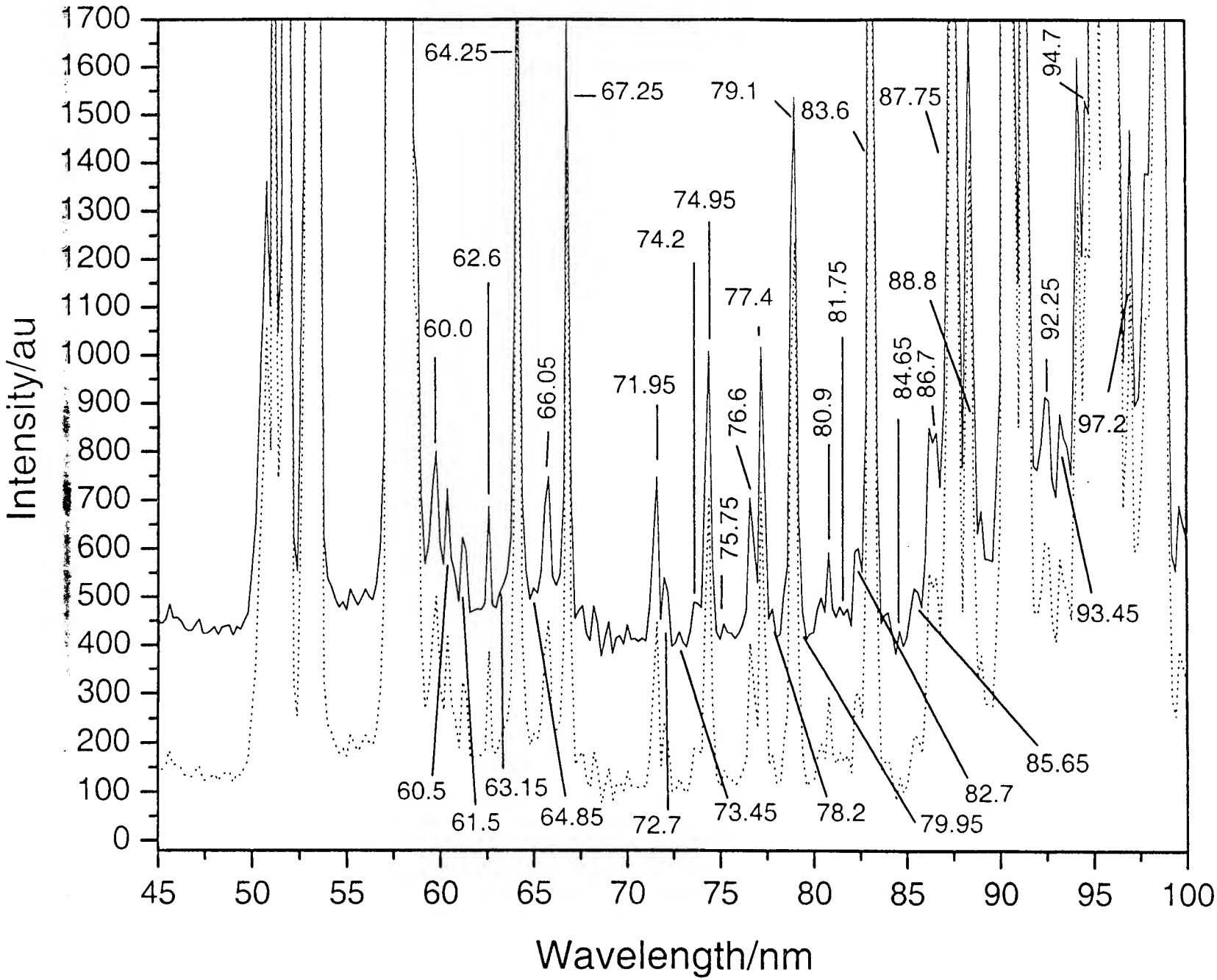
Intensity/au
Wavelength/nm
1700
1600
1500
1400
1300
1200
1100
1000
900
800
700
600
500
400
300
200
100
0
45
50
55
60
65
70
75
80
85
90
95
100
64.25
67.25
79.1
83.6
87.75
94.7
74.95
74.2
62.6
77.4
88.8
60.0
81.75
92.25
66.05
71.95
84.65
86.7
76.6
80.9
97.2
75.75
93.45
60.5
63.15
61.5
64.85
72.7
73.45
78.2
79.95
82.7
85.65

Fig. 17

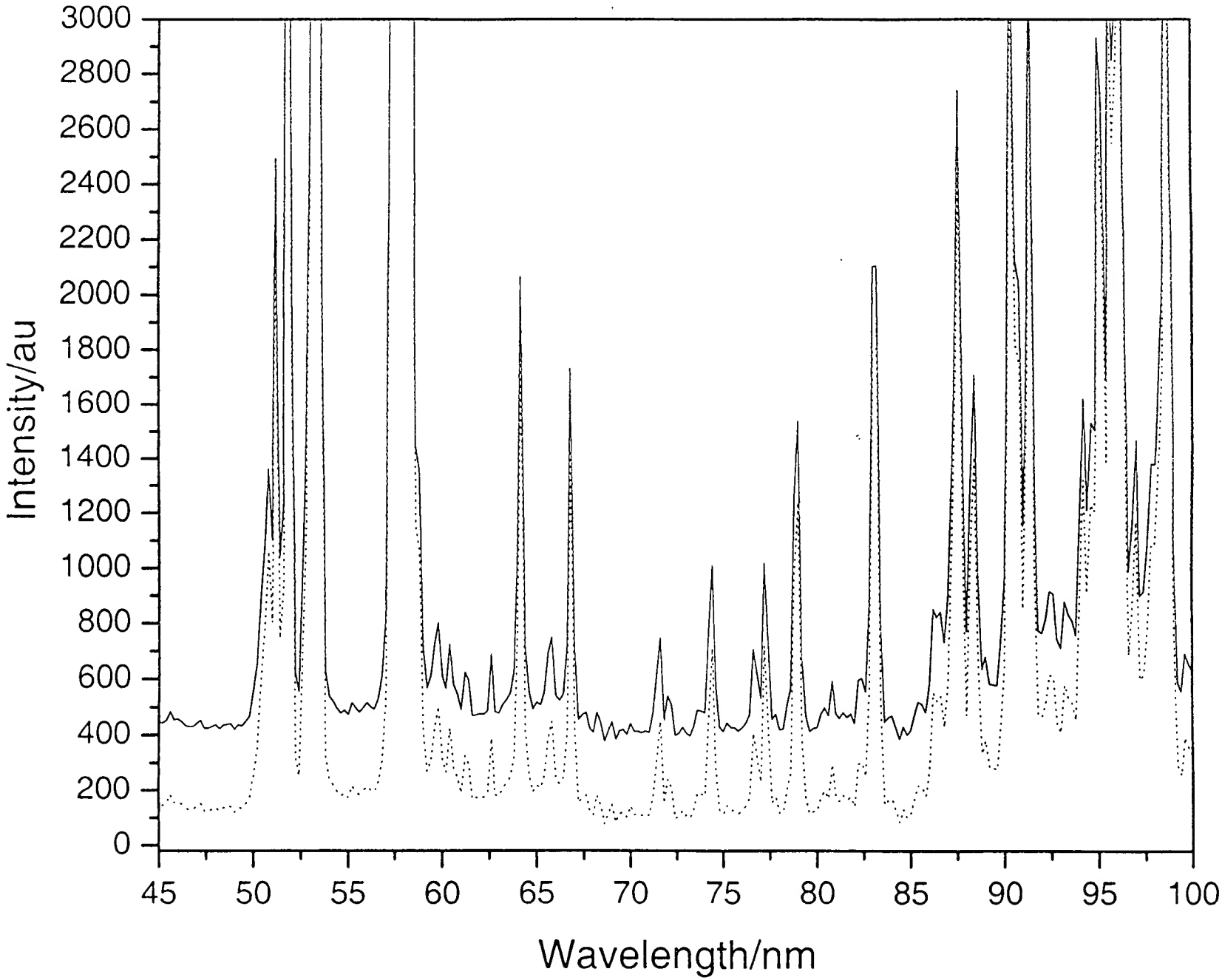
Intensity/au
3000
2800
2600
2400
2200
2000
1800
1600
1400
1200
1000
800
600
400
200
0
45
50
55
60
65
70
75
80
85
90
95
100
Wavelength/nm

Fig. 18

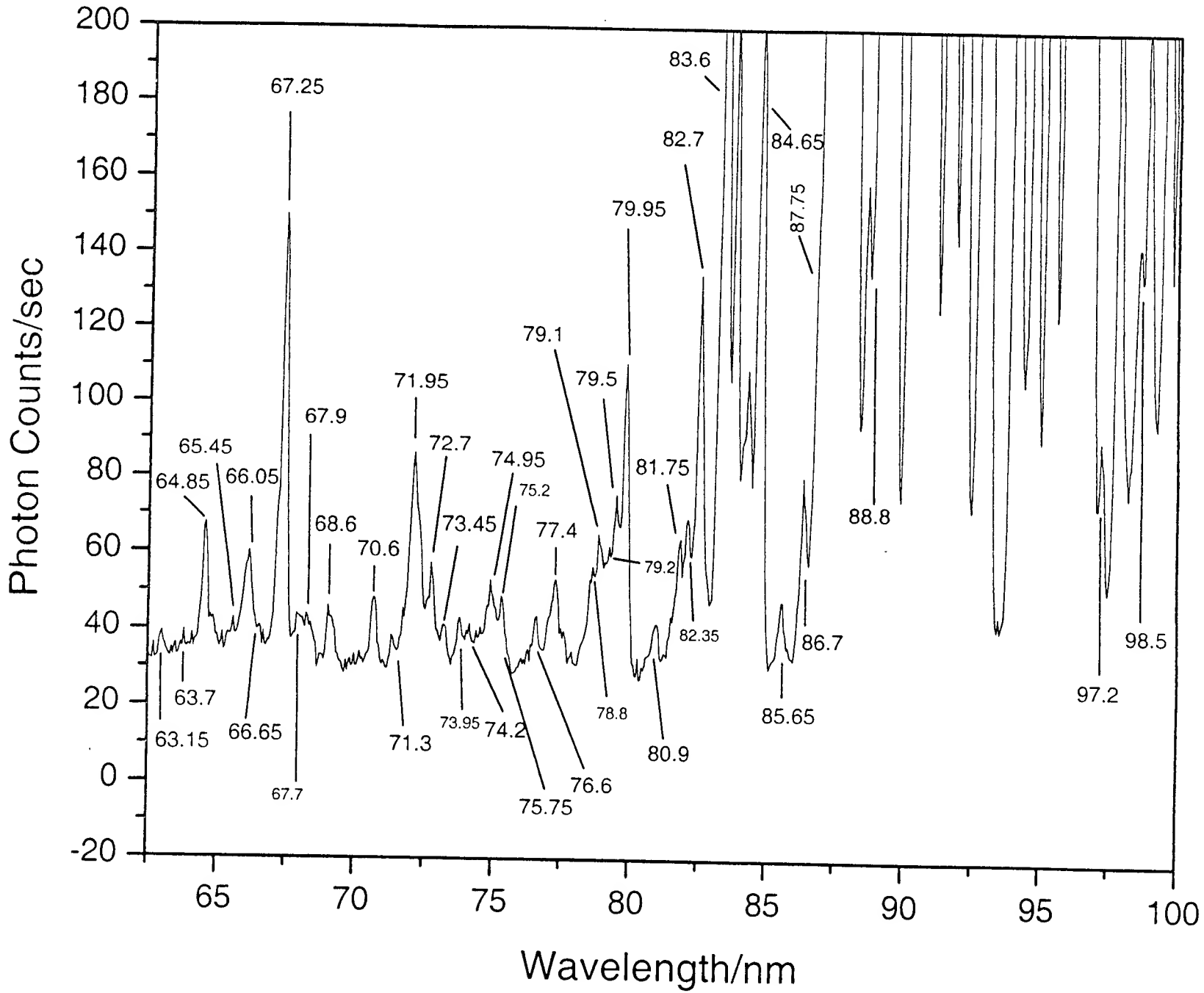
Photon Counts/sec
Wavelength/nm
200
180
160
140
120
100
80
60
40
20
0
-20
65
70
75
80
85
90
95
100
67.25
83.6
82.7
84.65
87.75
79.95
79.1
79.5
71.95
67.9
72.7
74.95
75.2
81.75
65.45
64.85
66.05
68.6
73.45
77.4
70.6
79.2
88.8
82.35
86.7
98.5
63.7
63.15
66.65
67.7
71.3
73.95
74.2
75.75
76.6
78.8
80.9
85.65
97.2

Fig. 19

Fig. 20

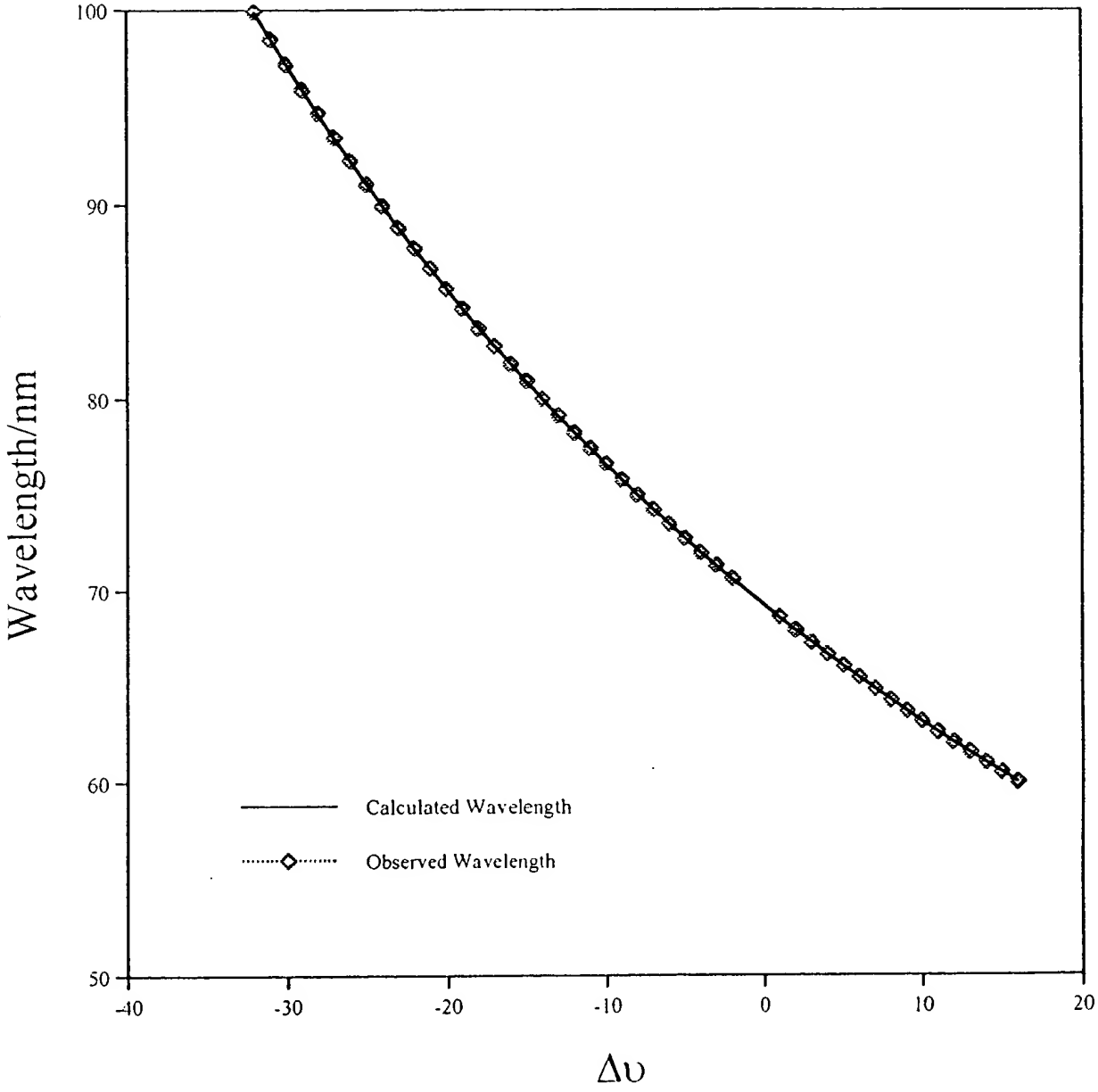
100
90
80
70
60
50
Wavelength/nm
-40
-30
-20
-10
0
10
20
Δυ
Calculated Wavelength
Observed Wavelength

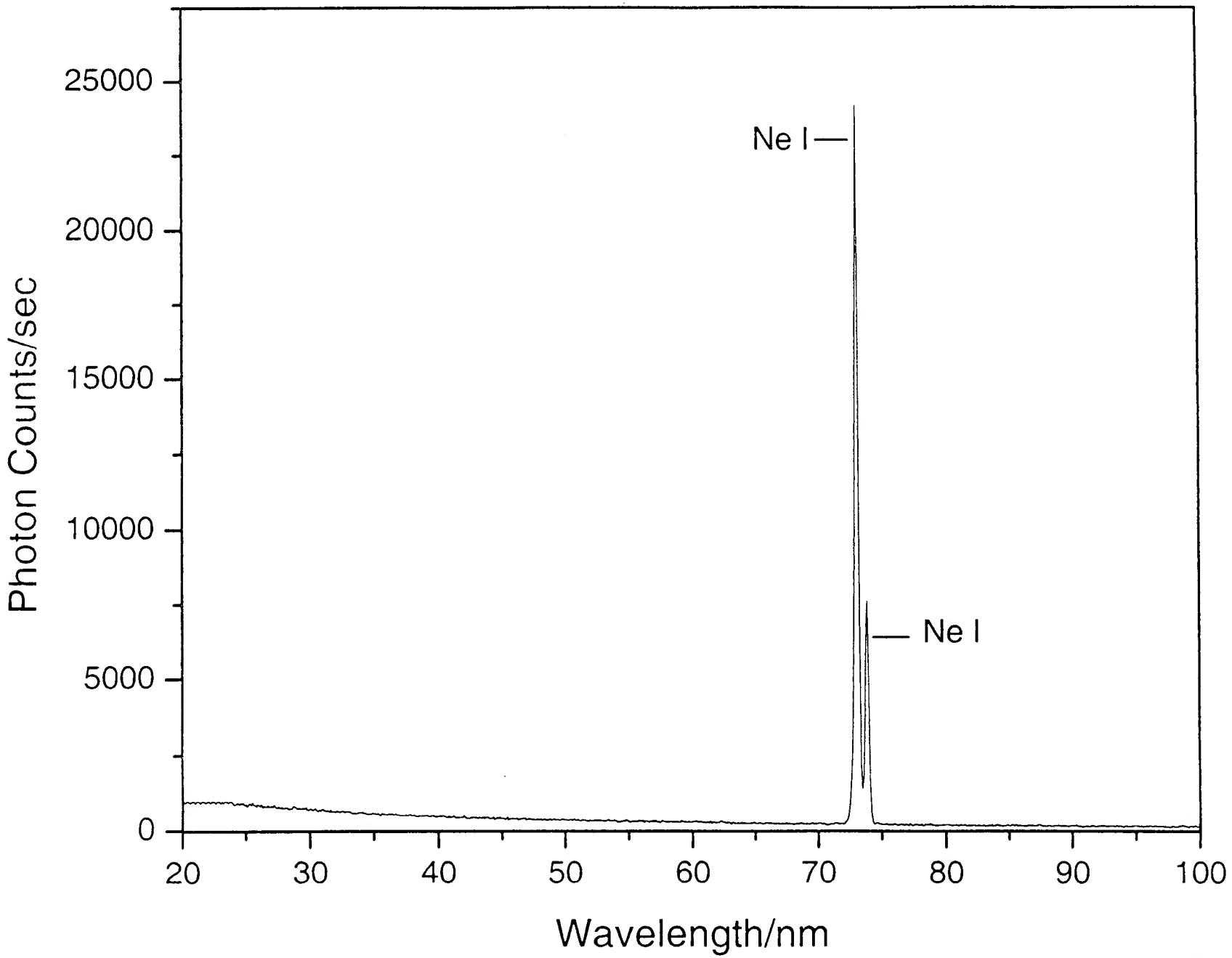
25000
20000
15000
10000
5000
0
Photon Counts/sec
Ne I
Ne I
20
30
40
50
60
70
80
90
100
Wavelength/nm

Fig. 21

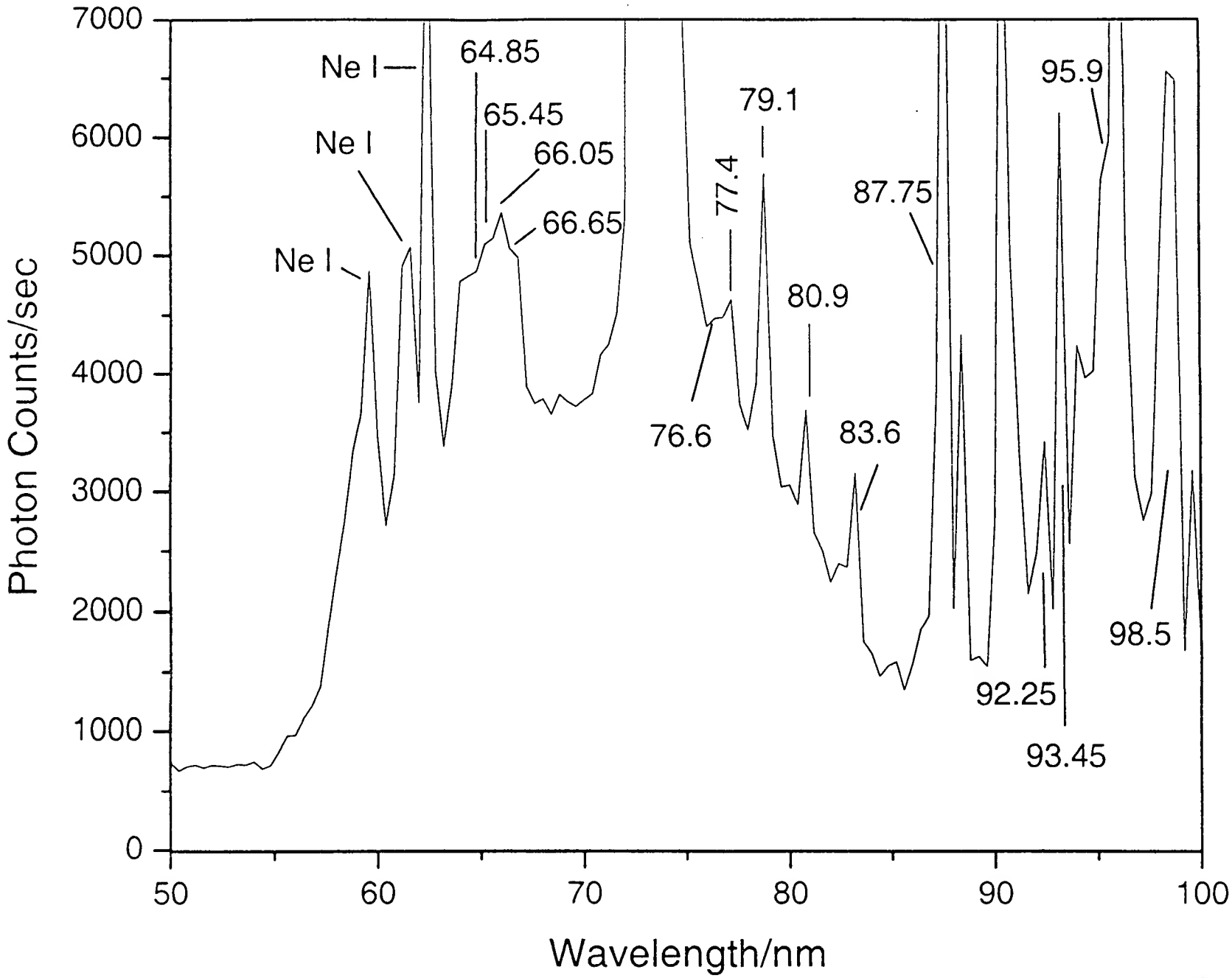
7000
6000
5000
4000
3000
2000
1000
0
Photon Counts/sec
50
60
70
80
90
100
Wavelength/nm
Ne I
Ne I
Ne I
64.85
65.45
66.05
66.65
77.4
79.1
76.6
80.9
83.6
87.75
92.25
93.45
95.9
98.5

Fig. 22

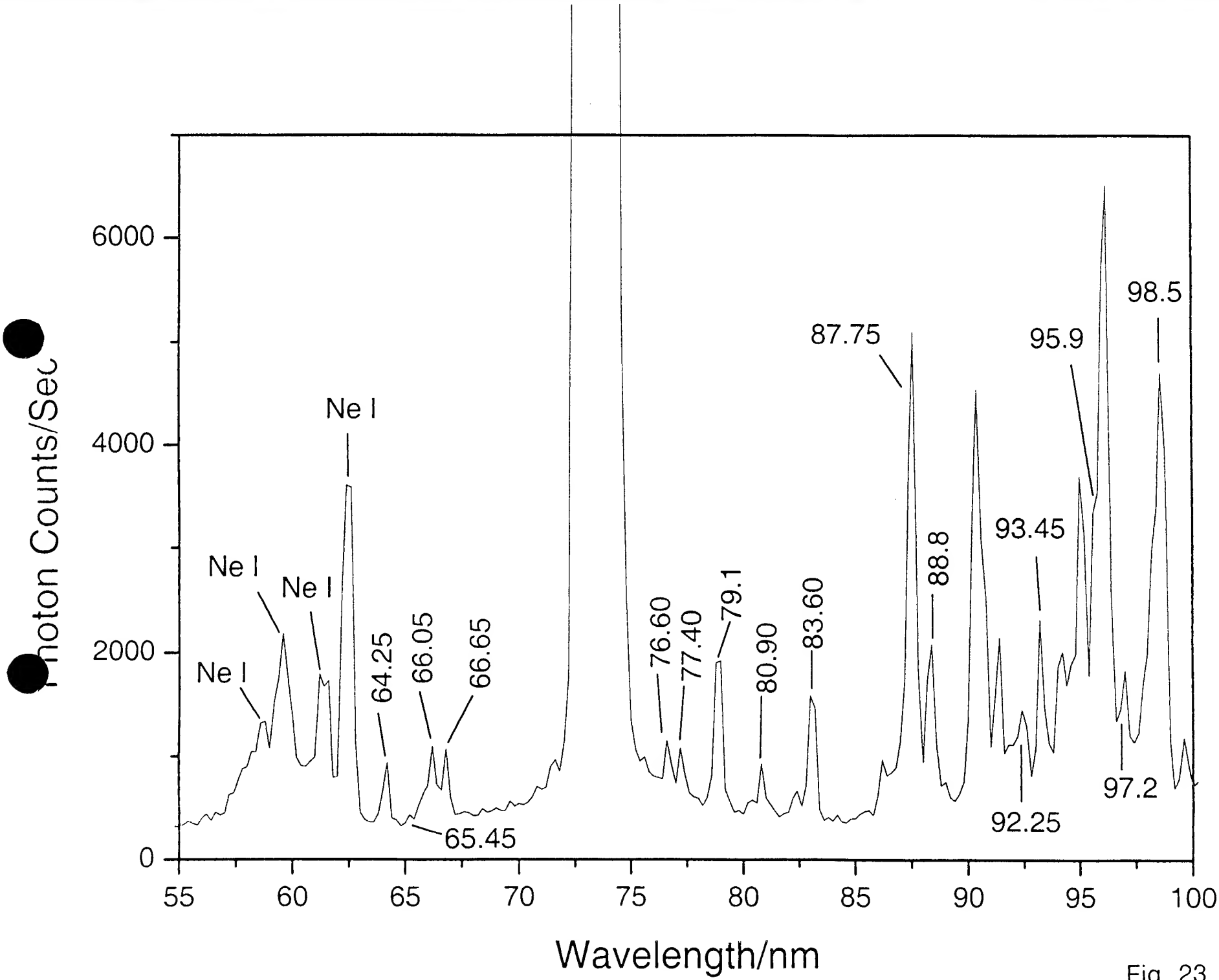
Photon Counts/Sec
6000
4000
2000
0
55
60
65
70
75
80
85
90
95
100
Wavelength/nm
Ne I
Ne I
Ne I
Ne I
64.25
66.05
66.65
65.45
76.60
77.40
79.1
80.90
83.60
87.75
88.8
93.45
92.25
95.9
97.2
98.5

Fig. 23

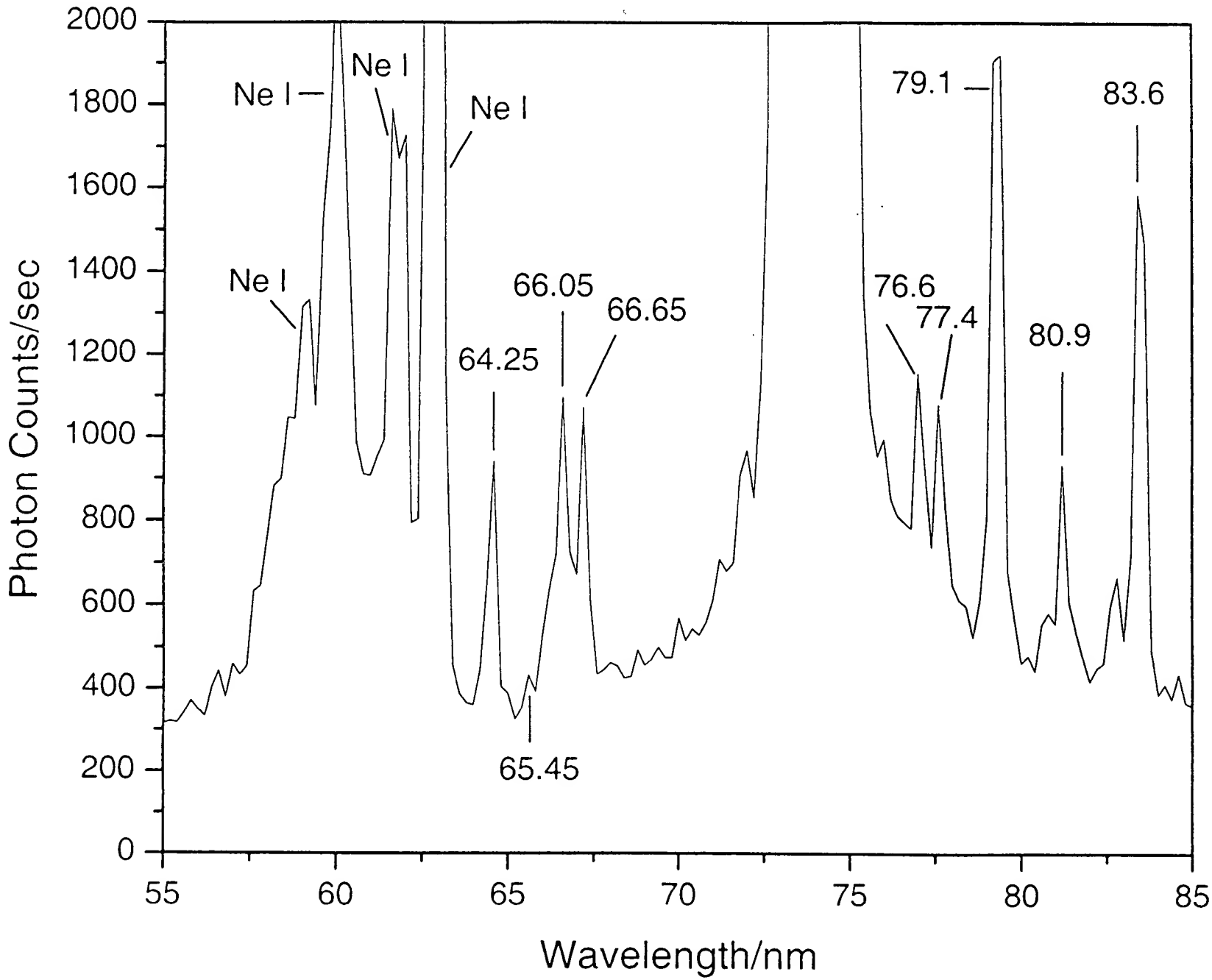
Photon Counts/sec
2000
1800
1600
1400
1200
1000
800
600
400
200
0
55
60
65
70
75
80
85
Wavelength/nm
Ne I
Ne I
Ne I
Ne I
64.25
65.45
66.05
66.65
76.6
77.4
79.1
80.9
83.6

Fig. 24

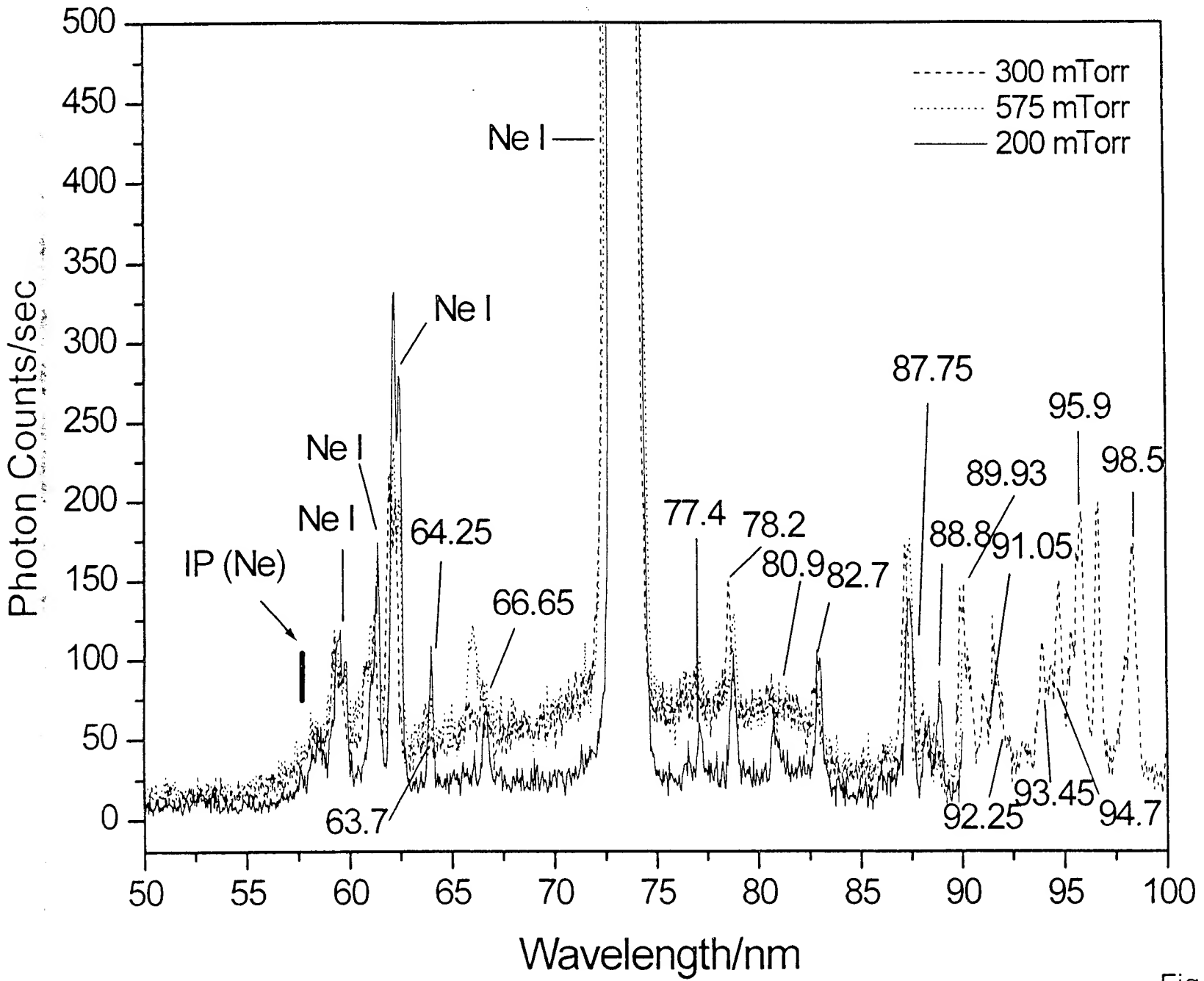
300 mTorr
575 mTorr
200 mTorr
Ne I
Ne I
Ne I
Ne I
IP (Ne)
64.25
66.65
63.7
77.4
78.2
80.9
82.7
87.75
88.8
89.93
91.05
92.25
93.45
94.7
95.9
98.5
Photon Counts/sec
Wavelength/nm
0
50
100
150
200
250
300
350
400
450
500
50
55
60
65
70
75
80
85
90
95
100

Fig. 25

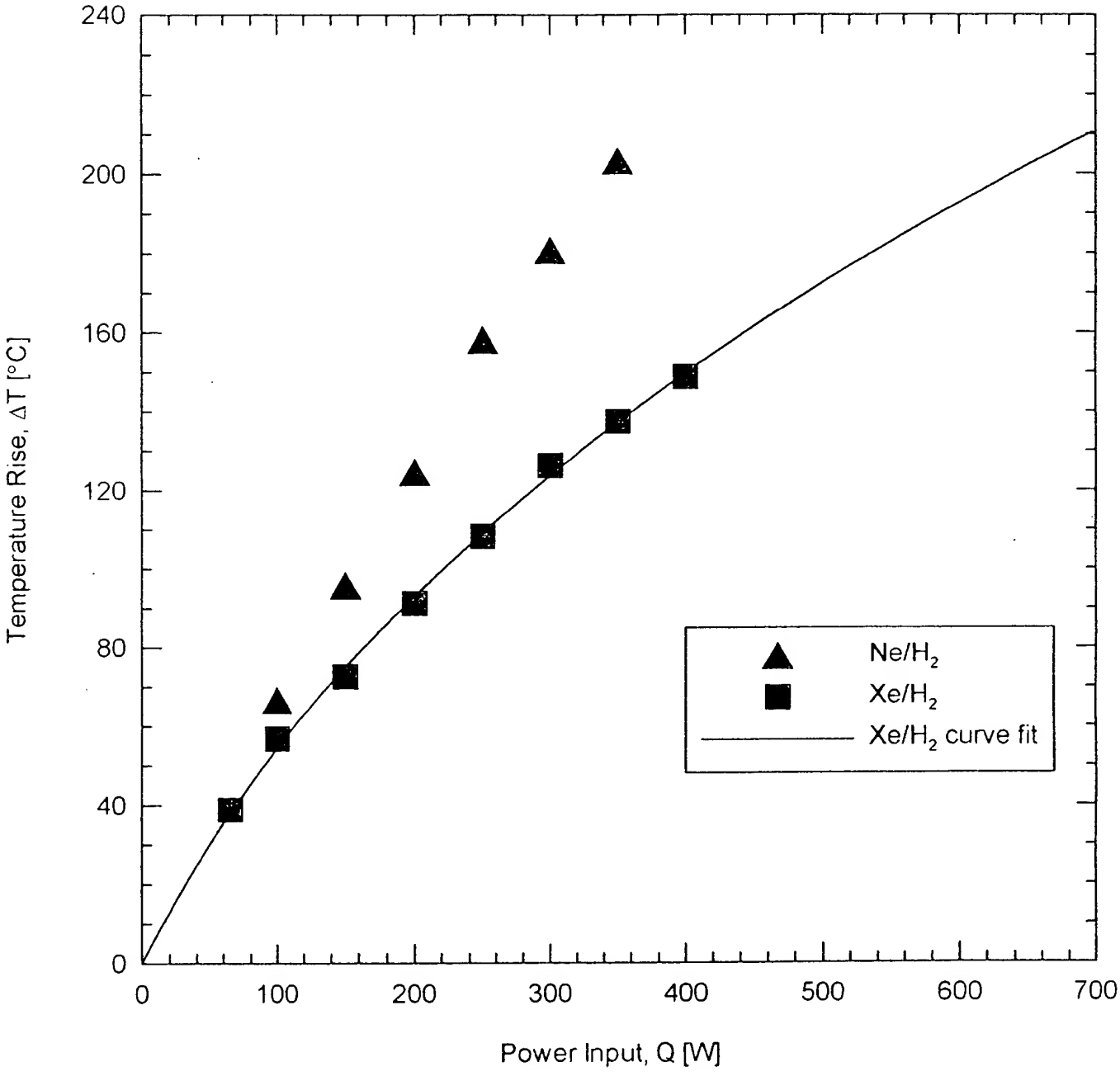
240
200
160
120
80
40
0
Temperature Rise, ΔT [°C]
0
100
200
300
400
500
600
700
Power Input, Q [W]
Ne/H2
Xe/H2
Xe/H2 curve fit

Fig. 26

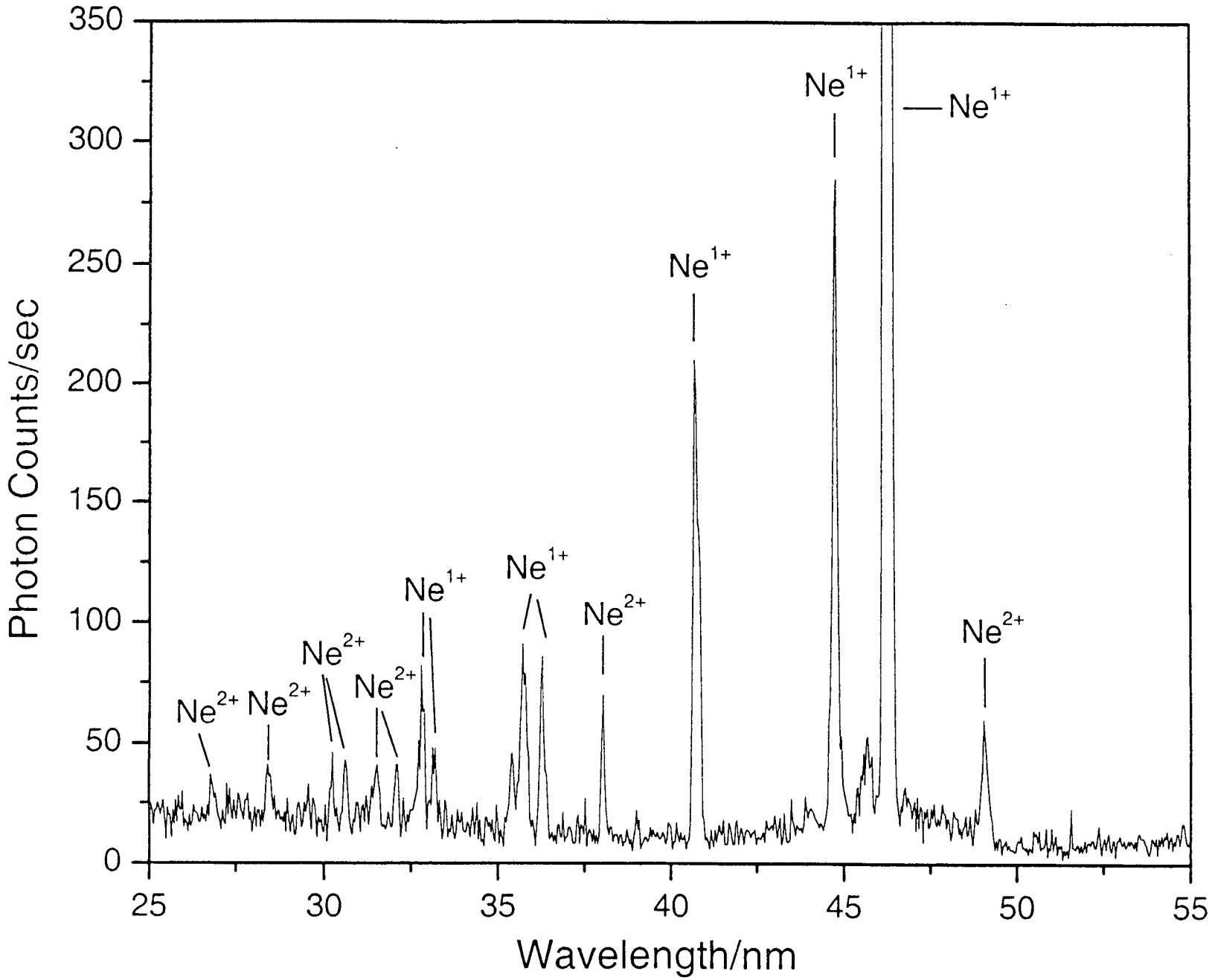
Photon Counts/sec
Wavelength/nm
350
300
250
200
150
100
50
0
25
30
35
40
45
50
55
Ne2+
Ne2+
Ne2+
Ne2+
Ne1+
Ne1+
Ne2+
Ne1+
Ne1+
Ne1+
Ne2+

Fig. 27